Chapter 3
Metal Nanoparticles for Microscopy and Spectroscopy

Peter Zijlstra, Michel Orrit and A. Femius Koenderink

Abstract Metal nanoparticles interact strongly with light due to a resonant response of their free electrons. These 'plasmon' resonances appear as very strong extinction and scattering for particular wavelengths, and result in high enhancements of the local field compared to the incident electric field. In this chapter we introduce the reader to the optical properties of single plasmon particles as well as finite clusters and periodic lattices, and discuss several applications.

3.1 Introduction

In the last two decades, nanostructured metals in the form of structured thin films and nanoparticles (NPs) have attracted attention from physicists and chemists alike as interesting materials for optics and spectroscopy. Metals do not intuitively stand out as particularly interesting materials for optics. Indeed, textbook physics tells that a perfect conductor simply expels any electric field, so that the only function of a metal should be to block light and act as a perfect reflector. Microscopically, this shielding of the bulk from any penetrating field is attributable to free electrons that provide a surface charge density on the metal surface to counteract any incident field.

P. Zijlstra (✉)
Faculty of Applied Physics, Eindhoven University of Technology, Den Dolech 2, 5612 AZ Eindhoven, The Netherlands
e-mail: p.zijlstra@tue.nl

M. Orrit
Leiden Institute of Physics, Huygens-Kamerlingh Onnes Laboratory, Leiden University, Postbus 9504, 2300 RA Leiden, The Netherlands

A. Femius Koenderink
Center for Nanophotonics, FOM Institute AMOLF, Science Park 104, 1098 XG Amsterdam, The Netherlands

C. de Mello Donegá (ed.), *Nanoparticles*,
DOI 10.1007/978-3-662-44823-6_3

This interpretation holds over a wide range of frequencies, from DC to well above the GHz range of current electronics. However, the free electrons intrinsically have a finite response time, above which they will not be fast enough to shield the bulk metal from incident fields. For typical metals the inverse of this response time, which is known as the 'plasma frequency', is around 500–1,000 THz. These frequencies correspond to electromagnetic waves in the visible and UV range.

Above the plasma frequency, a metal is not strongly reflective, but changes into a transparent material because the electrons cannot respond fast enough to screen the field. In most metals, the plasma frequency is in the ultraviolet, making them reflective in the visible range. Some metals, such as copper and gold, have inter-band transitions in the visible range, whereby specific wavelengths are absorbed yielding their distinct color. In the regime around and just below the plasma frequency metals are 'plasmonic'. As a consequence, small metal objects will support resonances of the free electron gas that strongly interact with light. For metal surfaces and metal sheets of submicron thickness, the free electron gas gives rise to resonances referred to as 'surface plasmon polaritons': surface waves at optical frequencies that are part photon (electromagnetic energy stored in electric field just above the surface) and part surface charge density wave. In this chapter we focus on a different type of plasmon resonance, namely localized plasmon resonances in nanoscale metal particles.

Gustav Mie [1] was the first to discuss in detail the peculiar optical properties of solutions of colloidal gold NPs, which have a ruby appearance. This color is tunable by particle size and shape (see Fig. 1.1 in Chap. 1), and is due to the resonant response of the 10^3–10^4 free electrons that a metal NP typically contains. Due to this resonant response, metal NPs are among the most strongly scattering solid state objects (when the scattering strength is normalized to the objects geometric cross section). In this Chapter we explain how this strong scattering comes about through the metal's dielectric function (Sect. 3.2) and how it can be tuned and optimized (Sect. 3.3). Owing to the strong electromagnetic fields that the ultra-tightly confined resonances support, the plasmon response is useful for a variety of spectroscopic applications ranging from sensing and label-free microscopy to enhancement of photophysical processes such as fluorescence and Raman scattering (Sect. 3.4). These properties that occur on the single particle level can be further manipulated and controlled by building small clusters or periodic lattices of plasmon particles using either lithographic methods or colloidal self-assembly techniques. In particular, coherences in scattering by multiple excited plasmon particles in clusters and lattices give further control over field enhancement and resonance linewidths of plasmonic structures, as well as a handle on directionality. This directionality expresses itself in the form of a strong dependence of a structure's local response on the direction from which the structure is illuminated, and conversely a strong anisotropy in light that is scattered or radiated by the structure. We discuss the physics of such plasmonic antennas in Sect. 3.5.

3.2 The Optical Response of Bulk Metals

The optical response of metal nanostructures is primarily determined by the metal's conduction electrons, which react collectively to external perturbations such as the applied electric field of a light wave. In this chapter, we are concerned with small particles and structures that are, however, large enough that the metal's response can be described by its bulk dielectric response. Deviations from the bulk response due to the small size of the nanoparticle are usually not observed above sizes of about 10 nm [2] (see Chap. 2, Sect. 2.4.2.1, for more details). Furthermore, it is assumed that the properties of the material close to the surface are identical to the bulk properties, and the lattice discreteness is disregarded. With these assumptions, and further neglecting quantum mechanical effects such as the spill-out of the electronic wave functions beyond the particle's surfaces, the metal can be represented by a continuous medium in classical electromagnetic theory. The metal is thus fully characterized by its complex dielectric permittivity $\varepsilon(\omega)$. In many cases, in particular for metals with a cubic lattice and for isotropic polycrystals, the permittivity tensor is isotropic and is therefore represented by a single function. It is important to realize that electromagnetism is a nonlocal theory involving long-range Coulomb forces, and that the response of free electrons in a metal particle is collective, i.e., it integrates all perturbations and boundary conditions imposed on the electronic system as a whole. This is in contrast to molecular systems or many semiconductor materials where each electron responds locally, independent from the boundary conditions at large distances.

3.2.1 The Drude Model for a Free Electron Plasma

Let us first consider the ideal case of a plasma of free electrons, i.e., a free electron gas whose electronic neutrality is ensured by a uniform and fixed distribution of positive charges. Those are carried by the heavy counter-ions, which can be taken as immobile in most cases. The free electron gas in a uniform positive charge density is called the jellium model [3]. Coulomb forces arise from the charge imbalance between the electron gas and the fixed jellium. They apply to the free electrons and tend to restore electric neutrality. For small displacements on large scales, the combination of restoring forces with electron inertia gives rise to harmonic oscillations around electric neutrality at the plasma frequency ω_P. As an easy argument to derive this characteristic frequency, consider a rod of metal with an volume electron density N. Suppose we displace all the free electrons by an amount x along the rod normal relative to the ionic backbone. As a consequence, on one end of the rod an excess layer of electrons arises, which represents a surface charge $\sigma = -Nex$, while on the other end of the rod the ionic backbone represents a positive but equally large surface charge. The surface charge sets up a homogeneous electric field $E = \sigma/\varepsilon_0\varepsilon_r$ that tends to pull the electron gas back to zero

displacement. According to Newton's equation, the motion of an electron will be governed by

$$m_e\ddot{x} = -eE = \frac{-Ne^2}{\varepsilon_0\varepsilon_r}x, \tag{3.1}$$

which is an equation of motion for a harmonic oscillator resonant at ω_P, given by

$$\omega_P = \sqrt{\frac{Ne^2}{m_e\varepsilon_0\varepsilon_r}}, \tag{3.2}$$

where e and m_e are the charge and effective mass of conduction electrons, N is their volume density, and $\varepsilon_0\varepsilon_r$ is the permittivity due to all other charges of the medium.

For noble metals such as gold and silver, with one conduction electron per atom, the electronic density is typically around $5 \times 10^{28}\,\mathrm{m}^{-3}$, which leads to a plasma frequency in the UV range. The plasma oscillation is damped by electron scattering off impurities, phonons, and surfaces. It is described phenomenologically by a viscous friction constant γ, whose inverse τ is called the Drude relaxation time and is of the order of some tens of fs in noble metals. This time is related through the Fermi velocity to a mean free path for electrons, which is of the order of a few tens of nanometers at room temperature.

By including only the free electrons' contribution to the polarization of a metal at frequency ω, we can derive the complex electronic permittivity $\varepsilon(\omega)$. To this end, suppose that we have an infinite block of metal and we consider the motion of a free electron when we drive the electrons with an oscillating electric field. The motion is governed by

$$\ddot{x} + \gamma\dot{x} = -\frac{eE}{m_e}e^{-i\omega t}. \tag{3.3}$$

If we solve for the *conductivity* $\sigma(\omega)$ of the metal which is defined through the relation between applied field E and induced volume current density j

$$j = -Ne\dot{x} = \sigma(\omega)E \tag{3.4}$$

we obtain the so-called 'Drude model' for the AC conductivity of a metal

$$\sigma(\omega) = \frac{\sigma_0}{1 - i\omega\tau} \text{ with } \sigma_0 = \frac{Ne^2\tau}{m_e}, \tag{3.5}$$

where τ is the Drude relaxation time. The Drude model describes the conductivity of metals such as gold, copper, and silver well over a very large frequency range, from DC (conductivity σ_0, with units of inverse Ohm-meters) to beyond the range of AC electronics, i.e., to optical frequencies.

In optics, the conductivity is an inconvenient parameter, as one usually deals with the permittivity $\varepsilon_0\varepsilon(\omega)$, and its square root, the refractive index $n = \sqrt{\varepsilon(\omega)}$. Using Maxwell's equation, in particular Ampère's circuit law in its microscopic and its macroscopic form, we can convert conductivity to permittivity, arriving at

$$\varepsilon(\omega) = 1 + \frac{i\sigma(\omega)}{\varepsilon_0\omega} = 1 - \frac{\omega_P^2}{\omega(\omega + i\gamma)}. \tag{3.6}$$

This description for permittivity is known as the 'Drude model'. Solving Maxwell's equations with this permittivity automatically takes all electromagnetic interactions between electrons into account. Therefore, whereas each electron responds individually to the local field it experiences, this field itself is determined by the collective response of all electrons. The Drude model captures the salient optical features of metals. For $\omega \ll \omega_P$ the dielectric constant is strongly negative. The limit of zero frequency and no loss ($\gamma = 0$), in fact corresponds to a 'perfect conductor', i.e., a medium that is completely impenetrable for electric fields. As the frequency approaches ω_P, the free electrons are less able to screen the incident field, and the field penetrates further into the metal. When $\omega > \omega_P$ the dielectric constant becomes positive and the metal becomes transparent.

3.2.2 The Dielectric Function of Ag and Au in Reality

Although the Drude model accounts for the main qualitative features of metal optics, modeling real metals requires including the response of the other, bound electrons. For example, the yellow color of gold in the visible range arises from the so-called interband transitions, which bring electrons from the filled *d*-bands to the open (*sp*) conduction band, above the Fermi level.

As shown in Fig. 3.1 for gold, interband transitions give rise to considerable deviations from the Drude model for wavelengths shorter than 600 nm by introducing strong losses for green and blue light. We must therefore consider the contribution of bound *d*-electrons to the optical properties to properly model the dielectric function of gold. Gold behaves as an excellent metal with very high conductivity only for wavelengths longer than 600 nm. For silver (Fig. 3.1), interband transitions peak for wavelengths around 310 nm and are negligible in the visible range. Silver presents a white shine and a flat and nearly total reflection throughout the visible and is well described by a Drude model. More accurate models of the optical properties of noble metal nanostructures and nanoparticles are often based on the measurements of optical constants by Johnson and Christy [4], for gold and silver, shown as data points in Fig. 3.1. Alternatively, one uses the values listed in the handbook by Palik [5].

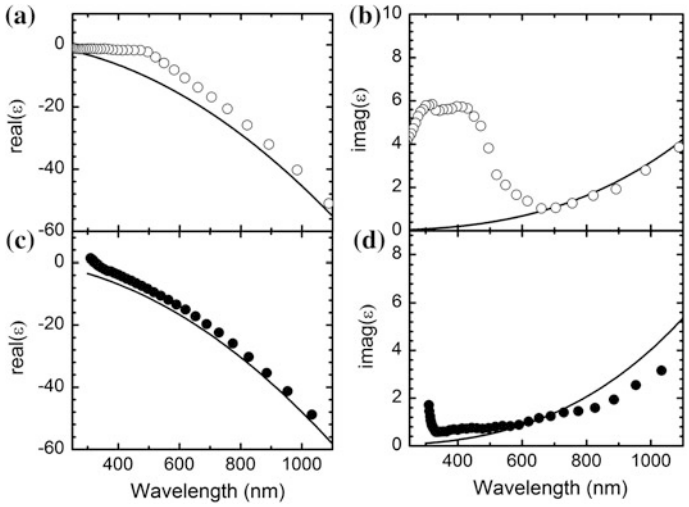

Fig. 3.1 Real and imaginary parts of the dielectric function of **a**, **b** gold, and **c**, **d** silver. *Solid lines* are deduced from the Drude model including only conduction electrons; the *symbols* represent measurements by Johnson and Christy [4] and include interband transitions. Drude parameters *gold* $\omega_p = 1.4 \times 10^{16}$ s^{-1} (or ~9 eV) and $\gamma \sim 0.01\ \omega_p$. *Silver* $\omega_p = 1.4 \times 10^{16}$ s^{-1} (or ~9 eV) and $\gamma \sim 0.003\omega_p$

3.2.3 Comparison of Metals

The interesting optical phenomena that we describe in the remainder of this chapter take place for visible and infrared wavelengths provided two conditions are met. Firstly, the plasma frequency has to be in the blue/UV part of the spectrum, since plasmonic resonances of nanoobjects usually occur just to the red of the plasma frequency. Secondly, damping must be low. The first requirement is met by most metals, including gold, silver, copper and aluminium. The second requirement, i.e., the low-loss requirement is met by only a few metals (see the handbook by Palik [5]). Indeed, DC resistivities of metals already show that damping is high except for the noble metals silver and gold, and possibly a few materials that are very difficult to handle, such as alkali metals. A further promising candidate is aluminium, which is suited for plasmonics in the UV. It has a plasma frequency at about 15 eV with a damping factor $\gamma \sim 0.02\omega_p$. It should be noted that the physics we describe below in principle scales to any frequency range provided one can shift the plasma frequency. For instance, many chemical compounds have a unique fingerprint in the mid IR and at THz frequencies. Since these frequencies are a factor 100 lower than optical frequencies, they require materials with 10,000 lower electron density in order to lower the plasma frequency. Such concentrations are achievable in doped semiconductors such as doped Si or materials such as InSb, which are being investigated for use in THz plasmonics.

3.3 Scattering by Small Particles

Because of the large negative value of the real part of the dielectric constant of noble metals, small particles present a large dielectric contrast with their surroundings, which usually have positive dielectric permittivity. This large contrast leads to strong scattering of light, which is often used for the detection and study of metal NPs. Scattering increases when the particles are dispersed in media with higher refractive indices, a phenomenon known as the immersion effect (pp. 37–40 in [2]). In the following, we discuss the scattering of a small sphere in the electrostatic dipole approximation. Section 3.3.1 deals with the polarizability of nanospheres, while Sect. 3.3.2 describes observables in scattering experiments. Section 3.3.3 discusses non-spherical particles, in particular spheroids.

3.3.1 Polarizability of a Small Sphere

Mie's theory [1] of scattering by a sphere in a homogeneous and isotropic medium with a different dielectric permittivity provides exact solutions for the scattered and transmitted fields [6]. These solutions simplify considerably if the sphere is much smaller than the wavelength of light in the materials involved. In that case, it is possible to neglect the variations of the electromagnetic field over the sphere's dimensions and to replace the exact electric field by a static one, giving rise to an effectively dipolar response. To evidence that this is indeed the case, let us consider the classical problem of a sphere of radius a in a static homogeneous incident electric field of strength E oriented along z. In electrostatics, the field is minus the gradient of a potential Φ that satisfies the Poisson equation. We are looking for solutions of the following equations:

$$\begin{aligned} \Delta\Phi_{\text{in,out}}(r) &= 0 \text{ everywhere with} \\ \Phi_{\text{in}}(r=a) &= \Phi_{\text{out}}(r=a), \text{and} \\ \varepsilon_{\text{in}}\frac{\mathrm{d}\Phi_{\text{in}}(r=a)}{\mathrm{dr}} &= \varepsilon_{\text{out}}\frac{\mathrm{d}\Phi_{\text{out}}(r=a)}{\mathrm{dr}}, \text{while} \\ \lim_{\mathrm{r}\to\infty}\Phi_{\text{out}}(r) &= -Er\cos\,\theta. \end{aligned} \tag{3.7}$$

These equations assume (1) there is no free charge, (2) the potential is continuous across the sphere boundary, but (3) its slope jumps, while finally the potential far away from the sphere is simply that of the incident homogeneous field oriented along $z = r\cos\,\theta$. The jump comes from Maxwell's boundary condition $\nabla\mathbf{D} = -\nabla(\varepsilon\nabla\Phi) = 0$, and has as interpretation that the response of the free electrons in the sphere effectively form a surface charge layer at the sphere boundary. It is easy to check that:

$$\Phi_{\text{in}} = -Er\cos\,\theta + \left(\frac{\varepsilon_{\text{in}} - \varepsilon_{\text{out}}}{\varepsilon_{\text{in}} + 2\varepsilon_{\text{out}}}\right) Er\cos\,\theta = -\left(\frac{-3\varepsilon_{\text{out}}}{\varepsilon_{\text{in}} + 2\varepsilon_{\text{out}}}\right) Er\cos\,\theta \qquad (3.8)$$

and

$$\Phi_{\text{out}} = -Er\cos\,\theta + a^3\left(\frac{\varepsilon_{\text{in}} - \varepsilon_{\text{out}}}{\varepsilon_{\text{in}} + 2\varepsilon_{\text{out}}}\right) E\frac{\cos\,\theta}{r^2} = -Er\cos\,\theta + \frac{p\cos\,\theta}{4\pi\varepsilon_0 r^2} \qquad (3.9)$$

solve the problem exactly. The solution shows two facts. Firstly, *inside* the sphere, the induced field is homogeneous, and exactly along the applied incident field, but with a different strength $3\varepsilon_{\text{in}}/(\varepsilon_{\text{in}} + 2\varepsilon_{\text{out}})$. Secondly, *outside* the sphere the field is the sum of the incident field, plus a term that is exactly equal to the field of a dipole of strength p located at the origin. The electrostatic response of a sphere is hence identified with an induced dipole moment p, the magnitude of which is proportional to the incident field E. The constant of proportionality is termed *polarizability*, defined through $p = \alpha_0 E$.

Returning to Mie's solution for scattering by a sphere, we note that in case of spheres much smaller than the wavelength λ, the electrostatic result essentially carries over. As the scattering object grows in size, the Mie solution deviates from the electrostatic solution. So-called radiative corrections, which are small, can be added to the polarizability of the sphere to simulate scattering, assimilating the sphere to a dipole. For noble metals, the dipole approximation is usually very good for diameters less than 50 nm. For larger sizes, contributions from higher multipoles can be included, but electromagnetic calculations soon become indispensable when the particle or structure sizes become comparable to a quarter-wavelength. Metal NPs that are used in optics experiments typically have diameters smaller than 100 nm, implying that the electrostatic approximation is reasonable for most experiments.

To obtain the scattered fields in the dipole approximation, one can start from Mie's result and expand it for small volumes, neglecting all terms of order 2 or higher in volume. The scattered field is that of a dipole oriented along the polarization of the exciting light. Where the scattered field overlaps with the incident exciting field, it leads to an attenuation of the latter in the transmitted direction, called extinction. Extinction includes losses to the incident wave either because of scattering to other modes or because of true dissipation leading to heat production or to the generation of other wavelengths. The polarizability $\alpha_0(\omega)$ of a small sphere with volume V in the dipole approximation is given by:

$$\alpha_0(\omega) = 3\varepsilon_0 V\left(\frac{\varepsilon(\omega) - \varepsilon_{\text{m}}}{\varepsilon(\omega) + 2\varepsilon_{\text{m}}}\right), \qquad (3.10)$$

in agreement with the electrostatic analysis in Eqs. (3.8) and (3.9). Here we use $\varepsilon(\omega)$ to refer to the dielectric permittivity of the metal that we already discussed, while ε_{m} refers to the dielectric permittivity of the embedding medium.

The polarizability shows a resonance at the surface plasmon resonance (SPR, or hereafter plasmon for short) frequency ω_{SPR}, when the real part of its denominator cancels, i.e., for Re $[\varepsilon(\omega_{SPR})] = -2\varepsilon_m$. If we assume a Drude model for the metal, and assume a particle in air, the polarizability simplifies to a Lorentzian resonance

$$\alpha_0(\omega) = \frac{3\varepsilon_0 V \omega_{SPR}^2}{\omega_{SPR}^2 - \omega^2 - i\omega\gamma}, \tag{3.11}$$

with the resonance frequency at $\omega_{SPR} = \omega_P/\sqrt{3}$, i.e., at frequencies significantly red-shifted from the plasma frequency. For silver and gold, this estimate results in plasmon resonances in the UV/blue part of the spectrum. The relation Re $[\varepsilon(\omega_{SPR})] = -2\varepsilon_m$ further also explains the sensitivity of the plasmon resonance to the surrounding index of refraction. Generally, the resonance red-shifts upon immersion in higher index media.

The electrostatic analysis of the field nearby a small sphere can be used also to estimate how strongly the incident electric field strength E can be enhanced due to the plasmon resonance. If we evaluate the dipole field exactly at the sphere boundary, where it is highest, we find

$$E_{\text{dipole}}(r = a) = \frac{p\cos\theta}{4\pi\varepsilon_0 a^3} = \frac{3\varepsilon_0 V}{4\pi\varepsilon_0 a^3}\left(\frac{\varepsilon(\omega) - \varepsilon_m}{\varepsilon(\omega) + 2\varepsilon_m}\right)E = \left(\frac{\varepsilon(\omega) - \varepsilon_m}{\varepsilon(\omega) + 2\varepsilon_m}\right)E. \tag{3.12}$$

To first order, the field enhancement is hence *independent* of the size of the sphere. On resonance Re $[\varepsilon(\omega_{SPR})] = -2\varepsilon_m$, then the ratio of dipole field to incident field reduces to

$$\left|\frac{E_{\text{dipole}}(r = a)}{E}\right| = \frac{3|\text{Re }[\varepsilon(\omega_{SPR})]|}{\text{Im }[\varepsilon(\omega_{SPR})]}. \tag{3.13}$$

Evidently, the lower the Drude damping rate of the metal, the higher the quality factor of the plasmon resonance as gauged from the resonance width in Eq. (3.11), and consequently, the higher the field enhancement. For a Drude metal, the field at the metal approximately reduces to ω_{SPR}/γ, i.e., to a factor 30 or so. Turning to a real metal, the field enhancement by a silver particle indeed approaches the Drude limit, whereas in gold the additional damping due to the interband transitions limits the enhancement to a factor ~ 5.

3.3.2 Extinction and Scattering Cross Sections

The polarizability that we introduced above in principle describes the response of a metal sphere to incident light. However, in actual experiments, the induced dipole moment, or polarizability, is not usually the actual observable. Instead, in a typical

experiment one would irradiate a particle with a known intensity (units W/m^2), and measure how much power (units W) the object takes out of the incident beam [6]. The ratio between power and intensity has units of area, and is hence coined 'cross-section'. The so-called 'extinction cross-section' quantifies how much light a particle takes out of a beam, while the 'scattering cross-section' quantifies how much light a particle reradiates as scattered light. It should be noted that the units of area for cross-sections lend itself to a very graphical interpretation: if, for instance, the extinction cross-section exceeds the geometrical cross-section, this means that the particle is more efficient at casting a shadow than would be expected from its geometric size. On plasmon resonance, this 'efficiency' (cross-section divided by geometrical area) can reach values up to 10 for spheres and even more for elongated particles. Extinction and scattering cross-sections in the dipole approximation can be expressed in terms of the polarizability by

$$\sigma_{\text{ext}} = \frac{k}{\varepsilon_0} \text{Im}\ \alpha(\omega), \quad \text{and} \tag{3.14}$$

$$\sigma_{\text{scatt}} = \frac{k^4}{6\pi\varepsilon_0} |\alpha(\omega)|^2, \tag{3.15}$$

where $k = 2\pi\sqrt{\varepsilon_m}/\lambda$ is the wavevector of light outside the scattering sphere. Equation (3.15) is essentially the famous Rayleigh scattering law: for a small particle scattering scales inversely with the fourth power of wavelength, and with the square of the volume (sixth power of diameter). On the other hand, the extinction cross-section, which is related to the scattered field by the optical theorem [6], scales with volume only. Since the difference between extinction and scattering must be due to absorption, the scaling implies that for very small particles (i.e., smaller than 1/10 of the wavelength of light), the extinction is mainly determined by absorption, as is well known for colored molecular solutions. Scattering becomes more and more important for larger and larger particles. Therefore, to detect small particles, absorption or extinction is much more interesting than dark-field scattering, which is weak and easily obscured by experimental imperfections. Once particles are above approximately 100 nm in diameter, the extinction of a metal particle is mainly due to scattering instead of absorption.

By way of example, Fig. 3.2 shows absorption, extinction and scattering spectra of a 25 nm gold sphere placed in vacuum, and in water (n = 1.33). All lines show spectra calculated using a full Mie calculation, except for the dashed spectrum in the left panel, which is calculated using Eqs. (3.14) and (3.15). Agreement between the approximate model and the full calculation is good. For both approaches we have taken the measured dielectric constant of gold according to Johnson and Christy [4] instead of the Drude function. The calculated spectra are in good agreement with the experimental ones (see, e.g., Fig. 2.22, Chap. 2). Spheres of diameter between 10 and 50 nm show a resonance at a plasmon frequency of

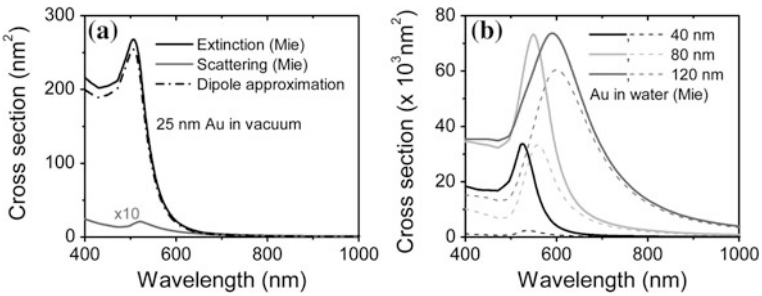

Fig. 3.2 *Left* cross section for extinction (*solid line*) and scattering (*grey line*) for a 25 nm diameter Au NP in vacuum, according to a Mie calculation. The dipole resonance at 507 nm is well captured by the dipole approximation. The on-resonance extinction cross section of $\sim$300 nm^2 is almost entirely due to absorption (the *grey curve* 'Scattering' was multiplied by a factor 10). *Right* Mie cross sections for extinction (*solid lines*) and scattering (*dashed*) for 40, 80, and 120 nm Au NPs in water. The water shifts the plasmon resonance to 520 nm for the smallest particles. The resonance further redshifts with increasing NP size, due to retardation effects not contained in the simple electrostatic model. For larger NPs the extinction is mostly due to scattering (*dashed line* close to *solid line*), and not to absorption (difference between solid and *dashed line*). For silver NPs as much as 95 % of the extinction can be due to scattering

around 520 nm. This resonance is broadened by losses due to the interband transitions. For 25 nm diameter spheres the absorption cross-section at the maximum is about 300 nm^2. We note that this explains the colors observed for colloidal suspensions of spherical gold NPs and their extinction spectra, which are nearly size independent for NPs smaller than 50 nm (Fig. 1.1, Chap. 1, and Fig. 2.22, Chap. 2). The color change between 50 and 20 nm (from red to orange, Fig. 1.1) is caused by a very small shift in the maximum of the extinction peaks (a few nm, see Fig. 2.22). For sizes larger than 50 nm, this spectral shift becomes increasingly larger, since the extinction cross-section grows less than linearly with volume and the absorption maximum shifts to lower frequencies (Fig. 2.22) because of corrections induced by retardation. This red-shift of the extinction peak leads to changes in the perceived color of the transmitted light, which gradually shifts from red to blue (Fig. 1.1).

The polarizability of a small NP can be corrected to include the effects of radiation by introducing an additional radiative damping channel, leading to a new polarizability [7]:

$$\alpha(\omega) = \frac{\alpha_0(\omega)}{1 - i\frac{k^3\alpha_0(\omega)}{6\pi\varepsilon_0}}. \tag{3.16}$$

A convenient shorthand for his relation is $1/\alpha(\omega) = 1/\alpha_0(\omega) - ik^3/6\pi\varepsilon_0$. The expression for the extinction and scattering cross-section in terms of the polarizability retain their validity with this revised polarizability, even for NPs with diameters up to 100–150 nm.

3.3.3 Spheroids

The analysis of spherical scatterers already contains all the generic physics of a plasmon resonance, the associated cross-sections, and the prediction of electric field enhancement. Yet, variations in particle shape offer significant control over these properties. For elongated particles such as nanorods, the particle is often approximated as an ellipsoid because there are analytical solutions for the polarizability of very small ellipsoidal nanoparticles. For ellipsoidal particles the depolarization field in the particle is uniform but not necessarily collinear with the applied field, which can be accounted for by incorporating a geometrical depolarization factor L in the dipole approximation [8]. The polarizability of an ellipsoid with volume V embedded in a homogeneous medium with dielectric constant ε_m can then be expressed as [2, 6]

$$\alpha_p = \varepsilon_0 V \frac{\varepsilon(\omega) - \varepsilon_m}{\varepsilon_m - L_p(\varepsilon(\omega) - \varepsilon_m)}, \tag{3.17}$$

where $p = (1, 2, 3)$ denotes the polarization of the incoming field along one of the principal axes of the particle. The dielectric function of the metal $\varepsilon(\omega)$ is given in Fig. 3.1 for different metals. The depolarization factors L_p depend on the elongation of the particle, and can be expressed as (for prolate spheroids) [2, 6]

$$L_1 = \frac{1 - e^2}{e^2}\left(1 + \frac{1}{2e}\ln\frac{1+e}{1-e}\right), \tag{3.18}$$

and

$$L_{2,3} = \frac{1}{2}(1 - L_1), \tag{3.19}$$

where L_1 ($L_{2,3}$) is the depolarization factor along the long (short) axis, and $e^2 = 1 - b^2/a^2$ is the eccentricity of a prolate (cigar shaped) ellipsoid with semi-major axis length a and semiminor axis length b. For a sphere the depolarization factors are 1/3 and Eq. (3.17) reduces to Eq. (3.10). Typical values for elongated particles are $(L_1, L_{2,3}) = (0.11, 0.45)$ for a prolate spheroid with an aspect ratio of 3. The optical cross sections of the particle are then given by Eqs. (3.14) and (3.15). The above equations give the optical properties of a single particle. For randomly oriented particles in a suspension, the optical cross-sections are simply given by the orientational average of the single-particle cross-sections.

Figure 3.3 shows examples of calculated absorption spectra for gold spheroids with different aspect ratios. An increasing aspect ratio results in a red-shifted longitudinal plasmon resonance due to a reduced restoring force on the oscillating electron cloud. This red-shift is also seen experimentally, as shown in Fig. 3.4. The transmitted light exhibits pronounced color differences due to the red-shift of the

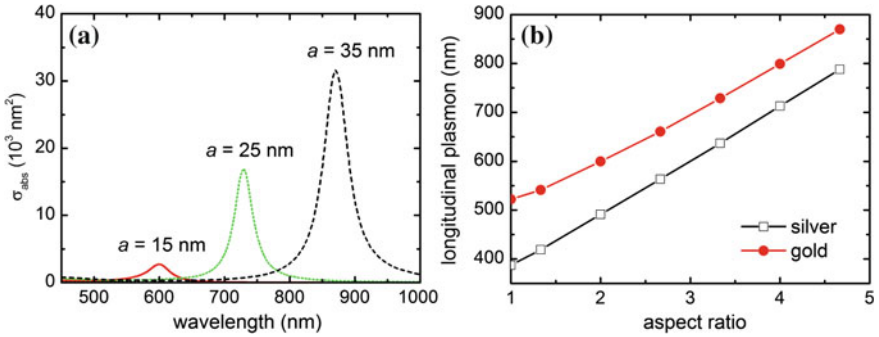

Fig. 3.3 **a** Calculated absorption cross sections of gold spheroidal NPs excited along their long axis. The NPs have a fixed semi-minor axis length (b = 7.5 nm) and varying semi-major axis length a. The dielectric constant of gold $\varepsilon(\omega)$ was taken from Ref. [4]. Note that the absorption cross section increases steeply because the volume of the NPs is different. **b** Longitudinal plasmon wavelength in the absorption spectrum of silver and gold prolate spheroids

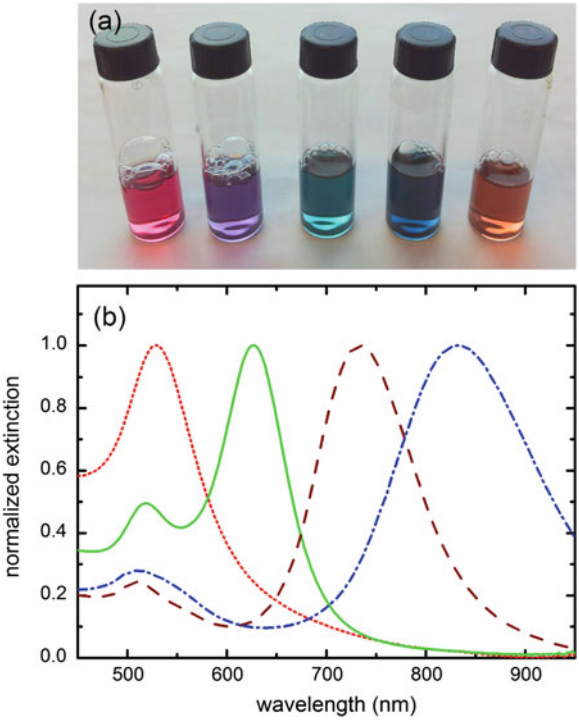

Fig. 3.4 **a** Photographs of colloidal suspensions of gold NPs with an ensemble average aspect ratio ranging from 1 (nanospheres, extreme *left*) to 4.5 (extreme *right*). The average diameter of the particles is ~20 nm and varies between the individual samples. **b** Normalized extinction spectra of colloidal suspensions of gold NPs with an ensemble average aspect ratio of 1 (nanospheres, *red dotted line*), 2.5 (*green solid line*), 3.5 (*brown dashed line*) and 4.5 (*blue dash-dotted line*). A clear red-shift of the absorption band is observed as the aspect ratio increases, which is responsible for the color changes observed in **a**

longitudinal plasmon absorption with increasing aspect ratio. As discussed above, for spherical Au NPs smaller than 50 nm the plasmon absorption occurs in the blue-green, hence the solutions appear red. For increasing aspect ratios the longitudinal plasmon resonance moves through the visible region to near-infrared wavelengths. For the largest aspect ratios the solutions appear brownish due to a featureless absorption profile in the visible with a small peak around the transverse plasmon resonance in the blue. Representative extinction spectra are shown under the photograph and confirm this interpretation (Fig. 3.4). Note that the linewidths in Fig. 3.4 are significantly broader than the calculated ones (Fig. 3.3). This is caused by inhomogeneous broadening due to the size distribution of the Au NPs.

The same effect is seen in silver nanorods (Fig. 3.3b), only here the plasmon occurs at a shorter wavelength due to the higher plasma frequency of silver. The transverse plasmon occurs at 520 nm for gold and at $\sim$400 nm for silver nanorods but is little affected by particle aspect ratio in the range of lengths we consider here. In the dipole approximation, nanospheres with diameters between 10 and 50 nm present a plasmon mode at about 520 nm (2.4 eV) for gold and about 400 nm (3.1 eV) for silver. We see from Fig. 3.1 that dissipation is weak for nanosphere plasmons in silver but not in gold. Gold exhibits intraband absorption at wavelengths between 200 nm and 550 nm, leading to additional losses for the plasmon. For gold nanorods of aspect ratios $a/b > 2$, however, the plasmon is shifted to wavelengths longer than 600 nm (2.08 eV), for which dissipation is weak. The plasmon dephasing time for gold nanorods is therefore longer than for gold nanospheres, resulting in a narrow plasmon linewidth [9]. This narrow plasmon of gold nanorods is useful for many applications that exploit the optical properties of a single particle, as we will discuss in the next section.

3.4 Applications of Single Metal Nanoparticles

Since the first far-field detection of single metal NPs in 1998, different applications have arisen that specifically rely on the optical detection of single particles [10]. Applications range from physical to biochemical and biological contexts. After a short introduction to the optical detection of single metal NPs we will highlight some of these applications, with the intention to give the reader insight into the current state-of-the-art. In Sect. 3.4.1 we firstly describe the basic principles of optically detecting a single metal particle. Then we discuss several applications including optical labeling and tracking (Sect. 3.4.2), optical trapping of single particles (Sect. 3.4.3), biosensing (Sect. 3.4.4) and the use of a single particle as a nano-antenna to enhance fluorescence (Sect. 3.4.5).

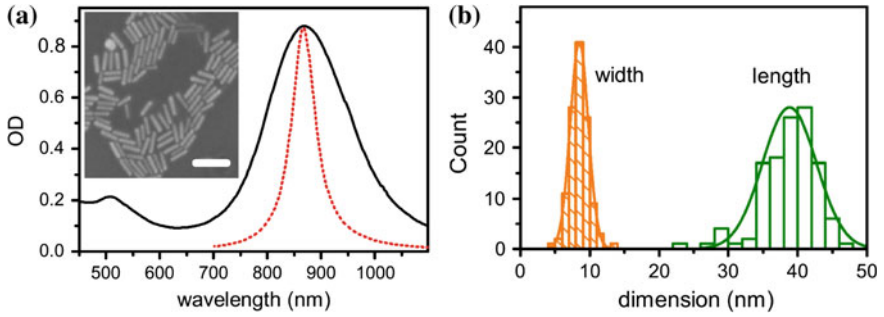

Fig. 3.5 **a** Extinction spectrum of an aqueous solution of as-prepared gold nanorods. The *inset* shows a scanning electron microscope image of a small volume of the sample that was drop cast on a silicon substrate. Scale bar 50 nm. To illustrate the inhomogeneous broadening of the optical spectrum we show the calculated spectrum of a single particle of 9 nm × 40 nm [Eq (3.17) inserted in (3.14)] as a *red dashed curve*. **b** Size distribution of the sample obtained from electron microscopy images as shown in **a**. Reprinted with permission from [10], Copyright (2011) Institute of Physics (IOP)

3.4.1 Optical Detection of a Single Particle

It is important to motivate why single particles bring new information, complementary to the more conventional measurements on ensembles. Although single-particle experiments are more difficult and provide a lower signal-to-noise ratio than ensemble measurements, they have distinct advantages:

(i) Even the best synthesis methods available produce a distribution of sizes and shapes (see Chap. 6 for details). Figure 3.5 shows the inhomogeneity of a colloidal sample of gold nanorods prepared by wet-chemical synthesis observed in an electron microscope and optically on an ensemble. By measuring the properties of individual particles, one recovers the full distribution of a variable in the heterogeneous ensemble.

(ii) The effect of small perturbations or changes in particle size, shape and composition, or in local surroundings can be measured with enhanced sensitivity due to the elimination of inhomogeneous broadening.

(iii) Single-particle experiments enable studies of rare but interesting objects, which would be difficult or impossible to extract or purify from an ensemble. Examples are the small assemblies of particles that are often used as antennas (see Sect. 3.5 below).

The most important component of a setup that is capable of detecting a single metal NP is the microscope objective lens. A high quality objective can focus the light to a diffraction limited spot, which is typically several hundreds of nanometers in diameter for visible light focused with a numerical aperture of about one. When combined with a stable light-source (either a laser source or a non-coherent

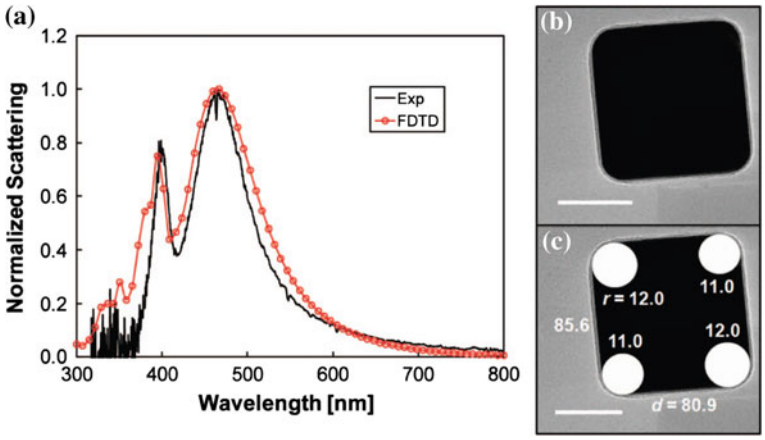

Fig. 3.6 Scattering spectrum and transmission electron microscopy image of the same gold nanocube. The electron microscopy image yields information about the morphology of the particle such as the edge-length and tip curvature, information that cannot be obtained from the spectrum alone. Scale bar 40 nm. Reprinted with permission from [13], Copyright (2009) American Chemical Society

broadband source such as a halogen lamp) and a sensitive detector, single particles can be studied in a variety of configurations, as will be discussed below.

Dark-field scattering: The most commonly employed configuration detects the light scattered by the metal particle on a dark background by using a commercially available dark-field condenser. This approach was first demonstrated in 1998 [11, 12] and has since been used to characterize the spectral and polarization properties of individual NPs. A powerful approach to correlate the morphology of the NP with its optical response is to deposit the particles on a conducting substrate (e.g. indium-tin-oxide coated glass). By imaging the same area on the sample in both an optical and an electron microscope the shape and size of the particle can be correlated to its plasmon spectrum [13] (see Fig. 3.6). This technique yields valuable information on the effects of minute differences in particle morphology (e.g. the endcap shape of a gold nanorod, the truncation of a triangular plate or cube, or the sphericity of a particle) on the plasmon resonance. Moreover, this correlation can definitively separate single particles from small clusters, something that is often difficult from the optical spectrum alone.

Bright-field detection: The scattered intensity scales as the squared volume of the particle (Eq. 3.15), making it difficult to image NPs smaller than 30 nm with dark-field scattering microscopy. In that case the scattered intensity is drowned by the noise level of a typical detector. Spectra of these small NPs are therefore better collected interferometrically in a bright-field setup [14]. Herein the scattered wave is overlapped with a reference wave, causing interference between the two. For convenience the reference wave is most often the reflection off the glass sample substrate, but it can also be a secondary beam. For small NPs the interference between

the reference and scattered wave results in a detected intensity that scales as the NP volume instead of the volume squared. This technique is capable of detecting NPs as small as 5 nm with a reasonable signal-to-noise ratio. Bright-field microscopy detects the NPs against a high background (the reference field) so it is important to use a stable light source to prevent fluctuations in the background intensity.

Photothermal microscopy: A complementary method that detects particles down to 1.4 nm and even single absorbing molecules is photothermal detection [15]. In photothermal microscopy a pump beam is absorbed by the particle, which subsequently heats up due to the efficient non-radiative decay of the excited electron-hole pairs. The thermal energy is dissipated into the environment, which causes a change in the index of refraction around the particle due to thermal expansion of the solvent. This so-called thermal lens is then detected by a secondary probe beam either in transmission or reflection. Because the probe beam wavelength is chosen far away from the plasmon resonance it is not absorbed by the NP, and much higher probe intensity can be used to reduce photon noise. The heating beam is time-modulated at a high frequency in the MHz range, and the resulting variations in the detected probe laser intensity are extracted with a lock-in amplifier. The photothermal signal thus detects a weak effect (the refractive index change) but by accumulating the contribution of many photons it can still achieve an excellent signal-to-noise ratio.

Photoluminescence: Photoluminescence (PL) microscopy is also capable of detecting a single metal NP. Luminescence detection is gaining popularity because the technique is analogous to fluorescence microscopy to image single organic fluorophores, and because highly sensitive setups are already available in many laboratories. The advantage of PL microscopy is that, since the luminescence wavelength is different from the excitation wavelength, it is in principle easy to separate signal from scattered background, simply using optical filters. The first observation of PL of gold dates back to 1969 [16], when Mooradian studied bulk gold and observed a broad PL spectrum with a quantum yield (number of emitted photons per absorbed photon) of about 10^{-10}. PL from bulk gold originates from radiative transitions of conduction electrons toward empty electron states, which can be either holes in the d-band (electron–hole interband recombination), or empty electron states or holes within the sp-conduction band (intraband transitions). Later studies showed that this low quantum yield can be enhanced by several orders of magnitude in the presence of surface roughness (lightning-rod effect) and localized surface plasmons. Recent studies have reported that the photoluminescence quantum yield of a single plasmonic particle only weakly depends on its size and shape and typically lies in the range of 10^{-5}–10^{-6}. Despite this low quantum yield single particles are easily detectable in a standard microscope due to their large absorption cross section. Under single-photon excitation, the luminescence brightness of a single metal NP of several tens of nanometers in diameter is comparable to that of a single fluorophore.

3.4.2 A Metal Particle as an Optical Label

Contrary to single organic fluorophores or semiconductor quantum dots the signal of metal NPs does not blink or bleach due to the large number of conduction electrons per particle (typically 10^3–10^5, compared to a single electron involved in fluorescence for an organic fluorophore). This gives metal NPs a considerable advantage over fluorophores when used as optical labels. The stable signals (scattering, luminescence, harmonic emission, photothermal) of metal NPs are hardly affected by their environment and allow for observation times only limited by diffusion out of the field-of-view of the microscope. Moreover, the high signal-to-noise ratio enables tracking of single metal NPs with microsecond time resolution. By tracking the particle in space and time one gains valuable information about the location and transport of proteins in living cells.

Once a metal NP is taken up by a cell either actively or passively, its strong scattering or luminescence can be used to track biomolecules attached to it. As an example, Fig. 3.7 shows the trajectory of a single 40 nm gold NP attached to a phospholipid [17]. The diffusion of the phospholipid in the plasma membrane of epithelial cells was monitored using differential interference contrast microscopy with a time resolution of 25 μs. Remarkably, the conjugate undergoes hopping diffusion between compartments in the membrane. To resolve the hop movement, the temporal resolution must be considerably better than the average residency time within a compartment (a few ms). The dwell time was thus not observable with the time resolution typical for imaging with organic fluorophores (viz., 33 ms).

In the crowded environment of a cell, the label size should be minimized to prevent effects of viscous drag on the process. Metal NPs of 10 nm and smaller

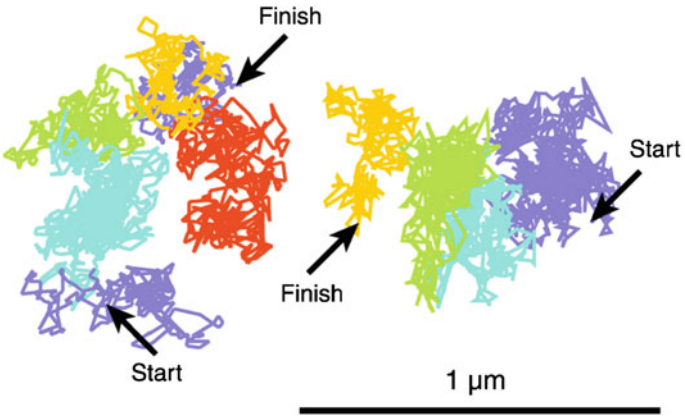

Fig. 3.7 Trajectories of two lipids in the cell membrane of an epithelial cell. The lipid was tracked by imaging a 40 nm gold NP attached to it with a time resolution of 25 μs. The different *colors* indicate the compartments through which the lipid diffused. Copyright 2002 Rockefeller University Press. Originally published in Ref. [17]

(no bigger than a large protein) cannot be detected with a conventional scattering-based setup and require a more selective method, such as photothermal microscopy (see Sect. 3.4.1 for details). In 2006 Lasne et al. [18] used this technique to track single gold NPs as small as 5 nm in a living cell. Even though the metal NP is small it still absorbs significantly more than the cellular background, enabling background-free detection inside the cell. Trajectories of a single particle can be recorded at video rate by employing a triangulation procedure yielding a localization accuracy of ~ 10 nm, comparable to state-of-the art super resolution microscopy techniques. With anisotropic NPs, one may not only track and measure translational motions of biomolecules, but also extract information on their orientation and rotation by exploiting the dipolar character of the plasmon resonance. Gold nanorods are often employed for two-dimensional orientation tracking due to their ease of synthesis and strong and anisotropic optical response. Assemblies of spherical NPs such as dimers also exhibit a dipolar optical response (Sect. 3.5), and have been used to track rotations.

As is evident from the above description, the ability to detect single metal NPs has led to exciting new insights in biophysical questions which are difficult to address with single organic fluorophores or semiconductor NPs. Passive tracking of single Au NPs has already yielded exciting results, but the active manipulation of particles for single-molecule force spectroscopy would immediately open a whole new realm of experimental possibilities. Recent developments in the optical trapping of single metal NPs have brought this prospect closer than ever, as will be described in the next section.

3.4.3 Optical Trapping

Optical trapping of a single metal NP can be accomplished by strongly focusing a near-infrared laser beam using a high numerical-aperture objective lens. The force exerted by the laser beam onto the NP consists of three components: the gradient force, the scattering force and the absorption force. The scattering and absorption forces scale as their respective optical cross-sections and act in the propagation direction of the laser beam. These forces therefore displace the particle along the optical axis and tend to push it out of the laser focus. The gradient force on the other hand stabilizes the position of the NP in the trap and can be expressed as

$$\vec{F}_{grad} = \frac{1}{2}\alpha'(\omega)\nabla\langle\vec{E}^2\rangle, \tag{3.20}$$

with α' the real part of the polarizability of the particle (see Sect. 3.3 for expressions for α in the dipole approximation) and $\vec{E}$ the electric field vector in the focus. Stable trapping can thus only be achieved when the axial gradient force exceeds the sum of the scattering and absorption forces. Maximizing the gradient force is often done by employing microscope objectives with a high numerical aperture. These objectives

focus the trap laser to the smallest possible spot-size (limited by diffraction), thereby maximizing the field gradient $\nabla\langle\vec{E}^2\rangle$ in Eq. (3.20). Note that trapping cannot be achieved with a laser wavelength on the blue side of the plasmon resonance because the polarizability, and thus the gradient force, is negative. The particles will then be propelled out of the laser focus.

It is immediately obvious that metal NPs can be trapped down to smaller sizes than dielectric particles. For example, α (in the dipole approximation, at 1,064 nm) is $\sim$10 times larger for a 40 nm diameter gold bead than for a polystyrene one. For an ellipsoidal particle of 70 nm × 20 nm this difference is as much as $\sim$50 times in the dipole approximation. As a result, single-beam optical tweezers allow for the stable optical trapping of single Au spheres and nanorods, and Ag NPs. For particles >100 nm forces in the pN range can be exerted with a laser power of several tens of milliwatts. This range of forces is promising for applications in single-molecule force spectroscopy, for example to stretch a single DNA molecule or to stall a molecular motor. Non-spherical metal NPs also experience a torque in an optical trap because of the anisotropy of their polarizability tensor. Au and Ag nanorods therefore align with the trapping laser polarization. The optical torque that can be exerted on a single Au nanorod was recently quantified to be $\sim$100 pN nm for 80 mW of trapping laser power [19], enough to twist biomolecules such as DNA. Although the absorption cross-section of the NP at the trap laser wavelength is small, it is non-negligible, and causes the NP to heat and eventually melt if the trapping power is sufficiently high. Typical heating rates of metal NPs in an optical trap are 0.1–1 K/mW, depending on the shape and size of the NP [19–21].

Force spectroscopy has now mainly been performed outside the cell, in a well-controlled environment. The main reason is that the dielectric particles often employed for these studies have diameters in the range of 500 nm–5 μm. These large particles are much bigger than typical organelles in the cell, and significantly distort cell function. Due to their large volume polarizability compared to dielectrics, the trapping of metal NPs seems a promising avenue to take single-molecule force-spectroscopy into the cell.

3.4.4 Biosensing

The frequency of the plasmon resonance is not only sensitive to the morphology and the composition of the particle, but also to the refractive index of its local environment. This sensitivity arises from the electric field associated to the plasmon, which extends beyond the particle's surface. The evanescent near-field penetrates the medium around the particle, making the plasmon resonance frequency sensitive to the refractive index in its immediate vicinity (Eq. 3.10). This index sensitivity opens up possibilities to optically detect molecules without the need to label them by using plasmon shifts as reporters for molecular binding. Remarkable progress has been made in the past two decades in the development of plasmonic biosensors. The commercial sensors do not contain metal NPs, but use thin metal

films that support propagating plasmon polaritons, optical excitations bound as a guided mode to the metal due to the free electron response. Propagating plasmonic biosensors are now commercially available to perform label-free interaction analysis with a high throughput and sub-nM sensitivity. However, large quantities of analyte are required to cover the surface of the sensor (on the order of a mm^2), which is problematic when expensive reagents are to be tested. The detection of only a few or even a single molecule is not possible because the response of the sensor is integrated over a large surface area. Plasmonic sensors based on single metal NPs are promising alternatives that do not suffer from these drawbacks.

Plasmon sensing can refer to one of two variations, namely (bulk) refractive index sensing and the sensing of molecular binding. In the former, only the bulk index sensitivity and linewidth of the plasmon determine the sensitivity. The sensitivity of a single particle sensor is often expressed in terms of its figure-of-merit (FOM), which can be expressed as

$$\mathrm{FOM} = \frac{\Delta\omega_{RIU}}{\Gamma}, \tag{3.21}$$

with $\Delta\omega_{RIU}$ the frequency shift of the plasmon for unit refractive index change, and Γ is the linewidth. The FOM is higher for narrower resonances because it is easier to determine peak-shifts. The FOM of different shapes of NPs has been widely investigated, and varies from $\sim$0.5–1 for a single Au sphere to $\sim$10 for a single Au nanorod. Gold nanorods are therefore widely used for sensing not only because of their high sensitivity but also due to the availability of straightforward protocols to synthesize (single crystalline) particles with a high yield. Bulk index changes of 10^{-2} cause a plasmon shift of several nanometers and are straightforward to detect using a single metal particle.

In the second case, when the binding of a (bio-)molecule is measured, the size of the NP is also of concern because it determines the spatial overlap between the local electric field and the analyte molecule. The local electric field decays approximately exponentially from the particle surface with a characteristic decay length that scales as the particle radius. The optimum NP size therefore depends on the volume of the molecule to detect, and generally smaller molecules require a smaller NP to achieve the highest sensitivity. Recently, such a single-particle plasmon sensor in the form of a single nanorod has allowed for the detection of binding events caused by a single molecule. Plasmon shifts can be monitored in time using for example photothermal microscopy [22] or dark-field scattering spectroscopy [23]. A typical time trace of the plasmon wavelength exhibits step-wise shifts caused by the binding and unbinding of single proteins to receptors on the surface of the NP (Fig. 3.8). Currently, label-free single-molecule detection is limited to proteins with a molecular weight > 50 kDa. These smaller proteins typically induce a plasmon shift of less than a nanometer, which is close to the noise level in a standard optical setup. Smaller molecules can still be detected by enhancing the plasmon shift [24]. The analyte can be coupled to a label with a high refractive index, for example another (small) metal NP (Fig. 3.8). Although the sensing is then not label-free

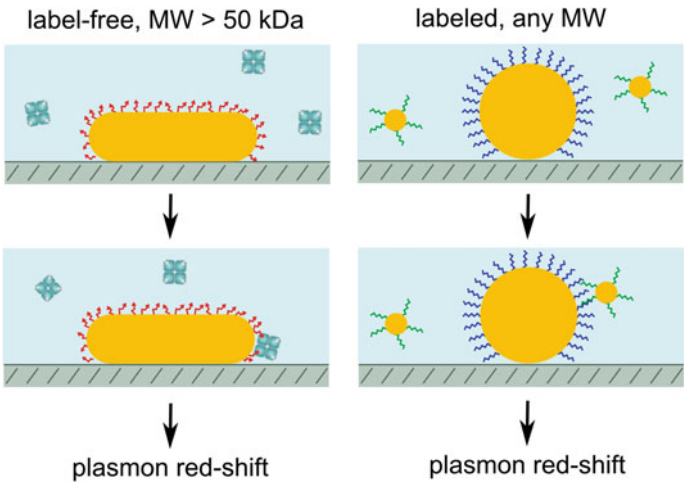

Fig. 3.8 Schematic showing current detection limits of biomolecular detection techniques that exploit the plasmon of a single NP. (*left*) The detection of large proteins (in this case streptavidin) can be accomplished by monitoring the plasmon of single gold nanorod, without the need to label the protein. (*right*) For smaller molecules such as DNA, the analyte (displayed in *green*) is usually labeled with a highly polarizable reporter particle to amplify the red-shift. The reporter particle in this example is a secondary gold nanosphere

anymore, the shift of the plasmon upon binding of the molecule can now be easily determined because coupling between the sensor NP and labeled analyte causes a dramatic plasmon resonance shift due to the hybridization of the plasmons in the NPs (see Sect. 3.5 for details on plasmon hybridization).

The proper functionalization of a metal NP allows for the specific detection of proteins, which is an important aspect of the development of functional biosensors. It is well-known that the highest sensitivity is reached at the edges of NPs (e.g. the tips of a nanorod), where the electric field strength is the highest. The functionalization of specific facets is therefore an effective avenue to improve the sensitivity of single-particle sensors. Protocols already exist to specifically functionalize the tips of nanorods [25] by introducing a surfactant in solution during the NP functionalization (Fig. 3.9). Surfactants assemble into dense bilayers on flat surfaces, but these bilayers are more open near asperities or on surfaces with a high curvature radius (such as the tips of a nanorod). Due to the reduced steric hindrance, thiolated receptors diffuse more effectively to the tips of the nanorod, where the field is highest. Also the edges and vertex sites of Au nanoplates can be selectively functionalized by a thiol-exchange reaction, which occurs preferentially at the edges of the Au NP again because of the reduced steric hindrance [26]. The above described optimization of the sensitivity is an active area of research that will eventually enable researchers to routinely detect individual molecules without the need for labeling.

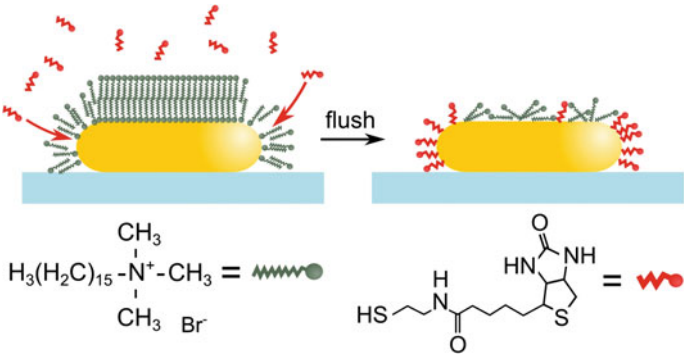

Fig. 3.9 Schematic showing the site-specific functionalization of gold nanorods. A dense bilayer of a surfactant (cetyltrimetheylammonium bromide, in *green*) provides steric hindrance that prevents the efficient functionalization of the side faces of a nanorod with thiolated biotin (*red*). This results in a particle that is mainly functionalized at its tips, which is also the area where the field-enhancement and thus the sensitivity to molecular binding is the highest. Note that the difference in surfactant density between the sides and the tip is exaggerated. Reprinted with permission from [25], Copyright (2012) Wiley-VCH

3.4.5 Emission Enhancements

Analogous to radio-frequency (RF) antennas, optical antennas efficiently convert free propagating optical radiation into localized energy, and vice versa. When an emitter, such as an organic dye or a semiconductor nanocrystal, is placed at the proper location in this high local field, the coupling between antenna and the emitter leads to enhanced single-fluorophore emission (Fig. 3.10). This enhancement near a plasmonic NP may arise from two factors:

(i) The lightning-rod effect (a non-resonant field-enhancement due to increased surface charge and crowding of electric field lines around sharp features) in combination with the presence of a surface plasmon leads to a high field enhancement in the vicinity of the NP. The excitation rate of the emitter can be enhanced by this high local field.

(ii) The antenna can also enhance the emission rate of a fluorophore. This Purcell effect arises from an enhanced density of optical states accessible for decay for a dipole, or, equivalently, from the enhancement of the dipole moment by electric currents in the NP antenna. The Purcell effect may not only change the intensity of the emission, but also its spectral shape, decay rate, and quantum yield. As metals also enhance non-radiative decay rates, they may also quench the emission [27] (Fig. 3.10). Quenching typically occurs for emitters placed within a few nanometers of the NP. The dipole field of the emitter then exhibits a strong field gradient at the location of the NP, causing the excitation of higher order plasmon modes. In contrast to the dipolar plasmon mode, higher order modes are poor radiators in small particles and

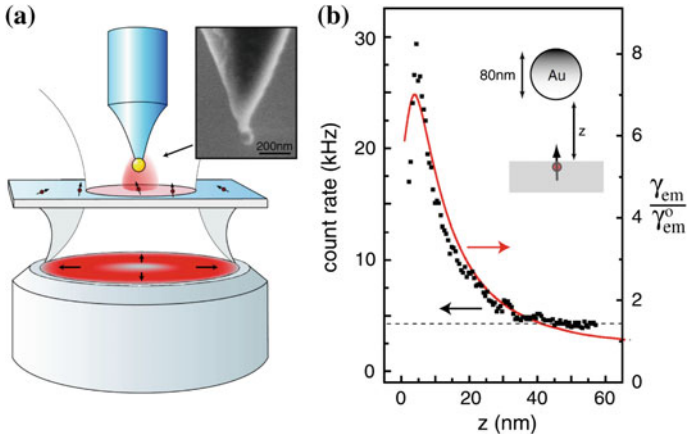

Fig. 3.10 **a** Optical setup used to characterize single-molecule fluorescence in the vicinity of a single 80 nm gold sphere attached to an optical fiber. **b** Fluorescence count-rate as a function of distance (z) between the fluorophore and the metal NP. The ratio between the emission rates in the presence (γ_{em}) and in the absence of the Au NP (γ^0_{em}) is also given (both enhancement and quenching are observed depending on z). Reprinted with permission from [27], Copyright (2006) by The American Physical Society

result in quenching of the fluorophores emission, and the energy is simply dissipated in the metal as heat. The balance between enhancement and quenching depends on the exact position and orientation of the fluorophore with respect to the NP, as well as on the NP size [28].

The main parameter that characterizes the emission enhancement is the magnitude of the local electric field, i.e. the degree to which the optical field is concentrated around the antenna (see also Sect. 3.3.1). For single NPs the field enhancements are modest: ~5 for a 20 nm Au sphere and ~50 for a 14 nm × 57 nm Au nanorod [29]. The field enhancement at asperities and metal tips can be significantly higher than for spherical particles due to the lightning rod effect (see above). Larger field enhancements are predicted in dimer junctions due to the hybridization of the plasmons of the two particles (see Sect. 3.5).

When assessing whether an antenna with its large field enhancement will enhance or reduce the brightness of a fluorophore, it is not enough simply to analyze the local field at the excitation and emission wavelengths. In addition, one has to take into account the intrinsic quantum yield (QY) of the isolated fluorophore. For "good" emitters (i.e., QY ≅ 1), any photon that is absorbed leads to exactly one output photon, and no further increase in QY is possible. Therefore, the antenna enhances brightness by increasing the effective excitation rate, directly resulting in a higher emission intensity (at least as long as no quenching of the emission occurs). In contrast, for "poor" emitters (i.e., QY << 1), the antenna can enhance both the excitation rate and the QY. A poor QY implies that for the isolated fluorophore the radiative rate is not competitive with nonradiative decay processes,

which are for instance enabled by the vibrational degrees of freedom in the emitter (organic fluorophores) or by Auger recombination processes (semiconductor nanocrystals). Accelerating the radiative decay through Purcell enhancement at fixed nonradiative decay rates means that radiative decay becomes more competitive, therefore effectively increasing the QY. Fluorescence intensity enhancements of 1,000 or more are easily reached when a poor emitter is positioned close to a single gold nanorod or a dimer antenna composed of two triangles in a bowtie-antenna configuration [30]. Nano-antennas therefore form a promising route to generalize single-molecule fluorescence imaging to emitters with low QYs.

Emission processes that scale nonlinearly with the local intensity profit enormously from the field enhancement around a nanoantenna. For example, surface enhanced Raman scattering (SARS) typically employs corrugations on a rough metal surface to enhance the Raman scattering signal, which scales as E^4. Enormous field enhancements of up to 10^3 are needed to amplify and detect Raman signals from single molecules. These enhancements are not easily obtained, and require selected asperities or sharp features on a rough metal film.

The large optical fields near a metal NP are also commonly employed for near-field imaging [31]. Near-field imaging is an approach to beat the diffraction limit in optical microscopy. The essential idea is that one of the ways to beat the diffraction limit of Abbe (resolution $\lambda/2NA$) to which far field optics are subject is to place a local nanoscopic reporter directly inside the sample under inspection. A plasmonic NP can be used as a near-field probe to interact locally with the sample. In a scattering based approach the evanescent component of the optical field at the sample is converted into propagating radiation by the scattering probe. By collecting this scattered radiation and mapping its strength, a spatial image can be collected by raster scanning the position of the probe. The region where the field is significantly enhanced is of the order of the size of the antenna, and sub-diffraction limited resolutions of 10–50 nm can be routinely achieved.

3.5 Clusters and Lattices of Metal Nanoparticles

While single NPs in isolation already provide a wealth of properties and applications, combining them into clusters or lattices provides even further benefits. When plasmonic NPs are brought together within distances of well below the wavelength, the plasmon resonances of the individual building blocks couple to form collective plasmon modes with novel properties. Following a seminal paper by Prodan et al. [32] this phenomenon is commonly known as plasmon hybridization. Plasmon hybridization allows to:

- Control at what wavelength collective plasmon resonances occur. Large shifts compared to the limited range of wavelengths achievable with just single particles are possible.
- Control the spectral linewidth of plasmon resonances.

- Introduce a strongly polarization dependent response.
- Achieve ultrahigh field strength.
- Control the directionality with which scattered light is reradiated.

In this section we first describe the concept of plasmon hybridization, and explain how spectral resonances can be tuned using hybridization (Sect. 3.5.1). Next, we validate the intuition of the plasmon hybridization approximation against exact calculations, and explain the relevance of plasmon hybridization for resonance linewidth (Sect. 3.5.2, applications in Sect. 3.5.3). In Sect. 3.5.4 the use of plasmonics to achieve ultrahigh field strengths is discussed. Directional antennas are treated in Sects. 3.5.5, and 3.5.6 finally discusses the extension of insights for finite clusters to infinite periodic lattices.

3.5.1 Plasmon Hybridization

By way of example, let us consider the physics of a plasmon dimer, a cluster of two identical plasmon particles with a volume V at a short center-to-center separation d from each other. In Sect. 3.3 we have established that a single plasmon particle responds to an incident field of strength $\boldsymbol{E}_{\text{in}}$ as a dipole with a dipole moment $\boldsymbol{p}$ set by a polarizability α that shows a clear resonance, according to (3.17). At very small separations d, one can approximate the field that the induced dipole $\boldsymbol{p}$ in a particle generates by its dominant near field term

$$\boldsymbol{E}_{\text{dipole}} = \frac{3(\boldsymbol{p}\cdot\boldsymbol{r})\hat{r} - \boldsymbol{p}}{4\pi\varepsilon_0 r^3} e^{-i\omega t}. \tag{3.22}$$

This equation contains the following physics: the scatterer oscillates at the same driving frequency ω as the incident field, falls off monotonically as $1/r^3$ as a function of distance r away from the center of the scatterer and has a distinct orientation dependence. On the axis along $\boldsymbol{p}$, the field is exactly parallel to $\boldsymbol{p}$, while on the axis transverse to $\boldsymbol{p}$, the field is antiparallel to $\boldsymbol{p}$ and twice weaker in strength. It is important to realize that this expression is approximate and only valid in the near field. Indeed, any radiating dipole also has a $1/r^2$ and $1/r$ field contribution that are both weaker at close range, but dominate further from the scatterer. Furthermore, at a distance larger than a fraction of the wavelength one should take into account that the radiated field is not everywhere in phase, but undergoes a retardation due to the distance it has to travel (replacing $e^{-i\omega t}$ by $e^{ikr-i\omega t}$). Suppose now that we quantify the response of a plasmon dimer where the dimer is illuminated with an incident field that is polarized along the dimer axis. Both particles will be driven directly by the incident field, and by each other. The responses of the two particles 1 and 2 hence follow from

$$\begin{aligned} \boldsymbol{p}_1 &= \alpha_1[\boldsymbol{E}_{\text{in}}(\boldsymbol{r}_1) + \frac{2\boldsymbol{p}_2}{4\pi\varepsilon_0 d^3}], \quad \text{and} \\ \boldsymbol{p}_2 &= \alpha_2[\boldsymbol{E}_{\text{in}}(\boldsymbol{r}_2) + \frac{2\boldsymbol{p}_1}{4\pi\varepsilon_0 d^3}]. \end{aligned} \tag{3.23}$$

Since the two particles will be polarized along the axis of the dimer, this coupling scenario is termed *longitudinal*. The above two equations can be rewritten in a matrix form as follows

$$\begin{pmatrix} 1/\alpha_1 & -2/4\pi\varepsilon_0 d^3 \\ -2/4\pi\varepsilon_0 d^3 & 1/\alpha_2 \end{pmatrix} \begin{pmatrix} \boldsymbol{p}_1 \\ \boldsymbol{p}_2 \end{pmatrix} = \begin{pmatrix} \boldsymbol{E}_{\text{in}}(\boldsymbol{r}_1) \\ \boldsymbol{E}_{\text{in}}(\boldsymbol{r}_2) \end{pmatrix}. \tag{3.24}$$

Substituting the Lorentzian form of the polarizability for each particle that is appropriate for a Drude metal (Eq. 3.11), one recognizes

$$\begin{pmatrix} \omega_{SPR}^2 - \omega^2 - i\omega\gamma & -6V\omega_{SPR}^2/d^3 \\ -6V\omega_{SPR}^2/d^3 & \omega_{SPR}^2 - \omega^2 - i\omega\gamma \end{pmatrix} \begin{pmatrix} \boldsymbol{p}_1 \\ \boldsymbol{p}_2 \end{pmatrix} = 3V\omega_{SPR}^2 \begin{pmatrix} \boldsymbol{E}_{\text{in}}(\boldsymbol{r}_1) \\ \boldsymbol{E}_{\text{in}}(\boldsymbol{r}_2) \end{pmatrix}. \tag{3.25}$$

We have now arrived at a linear set of equations that is formally equivalent to the physics of two pendulums that are coupled via the off diagonal term in the coupling matrix. In this analogy, the dipole moment $\boldsymbol{p}$ is equivalent to the pendulum amplitude, the driving force is the electric field $\boldsymbol{E}_{\text{in}}$ due to externally incident radiation, and the off-diagonal term essentially implies a coupling rate $6V/d^3\omega_{SPR}$. As in the pendulum case, this linear set of equations should be viewed as an eigenvalue problem, in which the eigenvalues $\omega_{\pm}$ correspond to the eigenfrequencies of the normal modes in the system. By bringing two identical plasmon particles close to each other, one expects the degenerate plasmon resonances to split into two distinct resonances. One of the resonances corresponds to a symmetric dipole configuration $\boldsymbol{p}_1 = \boldsymbol{p}_2$, where the dipole moments are aligned, while the second resonance corresponds to an antisymmetric configuration of dipole moments $\boldsymbol{p}_1 = -\boldsymbol{p}_2$. In analogy to the theory of hybridization of molecular orbitals, the symmetric mode is referred to as a *bonding* resonance, and the antisymmetric mode is called *antibonding*. The bonding mode is lower in energy, i.e., red-shifted relative to the bare plasmon frequency while the antibonding mode is blue-shifted. The eigenfrequencies (taking damping γ as zero) are

$$\omega_{\pm} = \omega_0\sqrt{1 \pm 6\frac{V}{d^3}}, \tag{3.26}$$

showing that the magnitude of the shift can be easily estimated by the dimensionless ratio V/d^3 of particle volume to the inverse separation cubed.

Figure 3.11 summarizes the level splitting in a graphical diagram. That the bonding combination is shifted to lower energy is intuitively understood simply by considering electrostatic energy arguments. Evidently, in the symmetric configuration, the

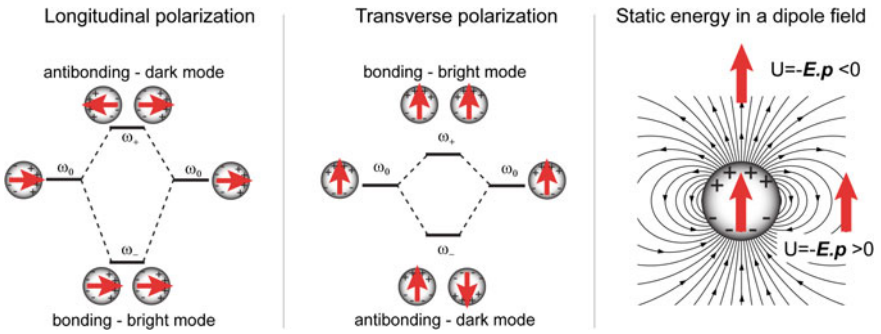

Fig. 3.11 (*Left panel*) Level scheme used to understand resonance hybridization in a plasmon dimer consisting of two identical particles in case of longitudinal polarization. (*Center panel*) Same in case of transverse excitation. The general intuition (*right panel*) is that the electrostatic interaction energy of a probe dipole in the field of a first dipole sets if a resonance redshifts or blue shifts. Whether a mode is bright or dark, simply depends on whether the total dipole moment vanishes, or is twice that of the single entities

dipoles are arranged head to tail, in such a fashion that each dipole moment is aligned with the field of its neighbor. Conversely, for the antisymmetric mode, a blue shift occurs due to the energy penalty that is associated with the antiparallel alignment of each dipole with the field of its neighbor. It should be noted in Fig. 3.11 that we have not drawn the energy splitting as symmetric around the unperturbed level. Firstly, this serves as a reminder that, different to first order perturbation theory for energy levels in quantum mechanics, in optics a square root enters (Eq. 3.26), which reduces the blue shift for large perturbations. Secondly, as the high-energy mode shifts towards the blue, the approximation that only the dipole mode contributes is increasingly violated, as the mode enters the range where the particles also have, e.g., a quadrupole resonance. Analysis including these multipoles indicates that the blue-shift is reduced compared to dipole intuition. Figure 3.11 also summarizes the level splitting for the so-called *transversely* coupled case. Suppose that we start from the same dimer, but that we illuminate it from a different direction and with a different polarization. If the incident field is polarized perpendicular to the dimer axis, both particles will obtain a dipole moment transverse to the dimer axis. The dipoles will again drive each other; however the interaction term reverses in sign and halves in strength for transverse coupling. In this case the symmetric eigenmode (dipole aligned) is blue shifted, while the antisymmetric eigenmode (antiparallel dipoles) is red shifted. In general, for illumination of a plasmon dimer under arbitrary polarization and incidence, a superposition of the longitudinal bonding and antibonding, as well as the transverse bonding and antibonding modes will be excited simultaneously.

This model is by no means rigorous, as it is limited to near field interactions, and a dipolar approximation. The intuition derived from hybridization will, however, generally be useful to interpret scattering spectra as well as exact numerical calculations, as long as we can consider plasmon particles to be small enough (radius $a \ll \lambda/2\pi$), close enough together for coupling to be via near fields (center-to-center

distance $d \ll \lambda/2\pi$), yet far enough apart that mutual driving yields no multipoles ($d > 2a$). Thus, plasmon hybridization has been applied to larger oligomers, clusters of anisotropic plasmon particles as well as 1D chains of particles at subwavelength spacing. Several authors have even used plasmon hybridization to understand more complex systems that do not have an obvious decomposition into dipolar scattering constituents. A prime example treated in the original work by Prodan et al. [32] is the core-shell NP that consists of a dielectric core, such as SiO_2, surrounded by a thin Au shell. If one views such a core-shell NP as the subtraction of a solid gold particle and a hole in a solid block of gold, one can view the shell resonances as a hybridization of the solid gold particle and the hole.

3.5.2 Validating Plasmon Hybridization Intuition

It is instructive to compare the simple formalism of plasmon hybridization as outlined above with the actual physics of coupled plasmon systems, as obtained from experiment or from rigorous calculations. Figure 3.12 shows rigorous calculations of the extinction of a plasmon dimer as a function of wavelength and as a function of separation, both for transverse and for longitudinal polarization [33].

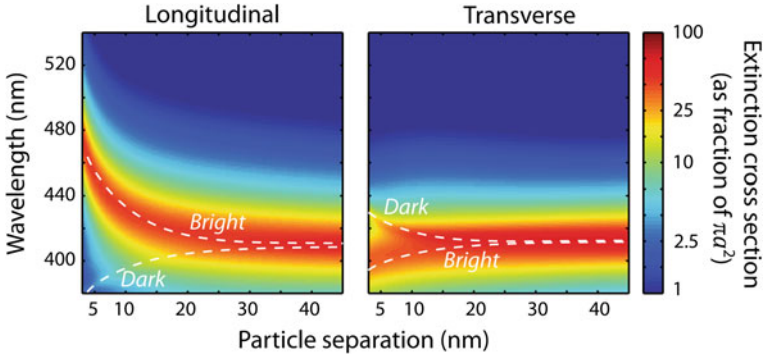

Fig. 3.12 Exact calculation using a generalized multipole expansion method of the extinction cross section of a plasmon dimer (NPs of radius a = 15 nm, embedded in a host of index 1.5, assuming a Drude model with $\hbar\omega p = 7.5$ eV and damping $\hbar\gamma = 0.05$ eV) for two excitation cases. The extinction cross section is normalized to the geometrical cross section of a single NP and plotted on a logarithmic color scale. *Left* excitation by a plane wave incident at almost normal incidence from the dimer symmetry axis, with polarization along the dimer axis. This polarization induces longitudinal dipole moments. The *left panel* hence shows the longitudinal hybridized resonances. At exact normal incidence the dark mode is not excited at all—at 10° off as in this calculation it is faintly visible. Right panel: excitation with polarization transverse to the dimer axis. By choosing an incidence angle at 45° off the dimer axis, both the bright and dark mode are excited. Note how the longitudinal case shows much larger frequency shift, and how the sign of the shift is reversed between the longitudinal and transverse (anti) bonding cases. *White dashed lines* are a guide to the eye. Calculations follow the method reported in [33]

The color scales clearly evidence the presence of two resonances that are degenerate at large separation, and split as the plasmon NPs approach. This basic result confirms the intuition gained by plasmon hybridization theory. For a quantitative comparison several hurdles need to be overcome.

The plasmon hybridization theory as we outlined above only predicts eigenfrequencies, and not the actual values of observables such as extinction. Nonetheless, the extinction calculated rigorously contains further features that we can qualitatively explain using the plasmon hybridization model. In particular we note that the two hybridized resonances are characterized by a highly unequal strength and a large difference in linewidth. To understand this difference we return to the arrangement of dipole moments that we identified as underlying the distinct resonances. Turning to the longitudinal resonance, the red-shifted mode corresponds to the symmetric combination $\boldsymbol{p}_1 = \boldsymbol{p}_2$ of dipole moments. This combination has a very large effective dipole moment $\boldsymbol{P} = \boldsymbol{p}_1 + \boldsymbol{p}_2 = 2\boldsymbol{p}_1$. Thereby, this mode radiates exceptionally well, and is easily excited using outside radiation. In contrast, the blue-shifted mode is antisymmetric $\boldsymbol{p}_1 = -\boldsymbol{p}_2$, and therefore has zero net dipole moment ($\boldsymbol{P} = \boldsymbol{p}_1 + \boldsymbol{p}_2 = 0$). The antisymmetric mode is hence a poor radiator. Moreover, it is not easily excited using external radiation, as it requires the incident field on the two closely spaced NPs to be applied out-of-phase. On basis of the magnitude of the total dipole moment, the symmetric longitudinal mode is called a *bright* plasmon resonance, while the antisymmetric mode is called *dark*.

In an extinction experiment, the difference between bright and dark plasmon resonances stands out in two ways. First, the bright resonance is most easily observed, due to the fact that coupling of the bright plasmon to incident radiation is strongest. Secondly, the bright and dark resonances have very different linewidths. The large difference in linewidth is easily understood if we consider the mechanisms by which the two eigenmodes lose energy. In case of the dark plasmon mode, the plasmon resonance only loses energy due to dissipation as heat as a consequence of the Ohmic damping of the metal. The damping of the dark plasmon can thereby be even less than the damping of the individual constituent particles: radiative damping that each NP may have is effectively canceled due to destructive interference of the radiated fields of the two dipole moments. Thereby the dark plasmon is referred to as "sub-radiant" (radiative loss lower than that expected for just one NP) and presents a rather narrow linewidth that is only limited by the Ohmic damping rate. Conversely, the bright plasmon loses energy both by Ohmic damping and by radiation damping. Owing to constructive interference of the radiated fields of the two dipole moments the radiative loss of the bright mode exceeds that of the individual NPs significantly. This effect is called *superradiant damping* and is easily understood as follows. Suppose we have N dipoles each with identical dipole moment $\boldsymbol{p}$. The radiated power is proportional to the total dipole moment squared and hence scales as $N^2|\boldsymbol{p}|^2$. The quadratic instead of linear scaling points to an interference effect that occurs when we coherently add the radiation of two dipoles. The fact that the loss *per dipole* increases proportional to N results in a broadening of the resonance, i.e., an increase in the radiative damping rate. For the dimer, the radiation damping doubles compared to a single particle.

3.5.3 Observation and Use of Dark Modes

Narrow linewidths could be especially desirable for spectroscopic and sensing applications. Firstly, when for instance sensing an analyte via frequency shifts, it is easiest to sense small shifts if the spectral feature that shifts is narrow. Secondly, by having lower loss and higher quality factors, dark resonances potentially store higher field densities in their near field. While dark modes can also be engineered in single NPs, i.e., by using higher multipole moments, plasmon hybridization provides a constructive design tool to engineer dark modes.

As a poignant illustration of the importance of dark modes that has been well studied in the plasmon literature, let us consider plasmon hybridization in a heptamer consisting of 7 plasmon NPs [34, 35]. This structure consists of a hexagon of NPs, surrounding a central one. Strictly speaking, since each plasmon NP has a 3-fold degenerate resonance (one for each axis), the heptamer has 21 normal modes. However, as the heptamer has the same symmetry as a benzene molecule, the 21 modes can be easily classified by symmetry. If we focus on modes that couple to excitation offered by in-plane polarized plane waves (as would be excited in a normal incidence optical experiment) only a small subset of eigenmodes participate. These are the combinations that in the vibrational spectroscopy of benzene would be coined 'infrared active'. Figure 3.13 shows the three infrared active eigenmodes that couple to *y*-polarized plane waves (in total there are 6 modes that couple to plane waves). The other 3 are obtained by a 90° rotation of all arrows in Fig. 3.13a). Due to the coupling between NPs, these three normal modes have both different eigenfrequencies and very different damping constants. The first mode has all 7 dipole moments approximately aligned and hence has a large damping

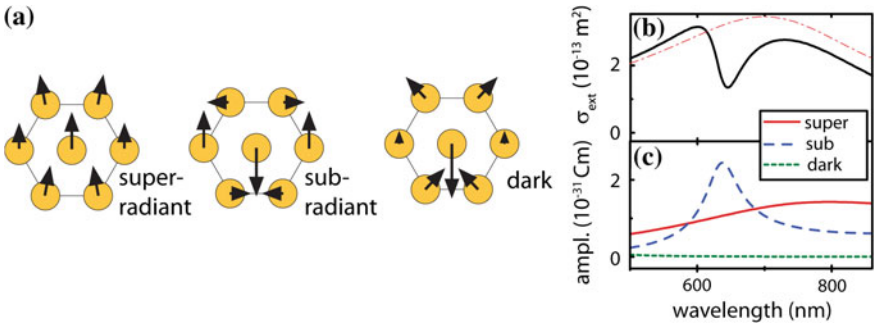

Fig. 3.13 Plasmon hybridization in a heptamer. **a** Arrows indicate the dipole orientation and strength for the three (out of 21) hybridized plasmon modes of a plasmonic heptamer (calculated for 100 nm Au NPs, spaced by 150 nm, in the irreducible representation E_{1u} that couples to normally incident plane waves with polarization oriented from *top* to *bottom* in this plot). **b** Extinction of the plasmon heptamer versus excitation wavelength. Dotted line indicates the extinction one would have in absence of the sub-radiant mode. **c** Amplitudes with which the three modes are excited (at 1 V/m incident field strength). Figure adapted with permission from [36]

corresponding to a 'bright' or 'superradiant' mode. The other two modes in contrast, have dipole moments that are not all parallel, and hence have a much smaller net dipole moment. One of these truly has zero net dipole moment and is hence 'dark'. The other has a residual net dipole moment that is not zero and is best described as 'subradiant'.

Figure 3.13b shows the calculated scattering spectrum of a plasmon heptamer [36] using a dipole model, which is in excellent agreement with, for instance, the experiment and full calculations of Hentschel et al. [35]. The scattering has a broad peak, due to the heavily damped superradiant mode. On top of this peak is a narrow feature, due to the subradiant mode. The one feature that is remarkable is that, although on the subradiant mode resonance the incident field causes a strong excitation of *two* modes instead of one, the scattering is *suppressed* and not enhanced. The physics is that of interference. The incident light drives a coherent superposition of two modes, which reradiate light out to the far field. The total scattered intensity is determined by the squared absolute value of the total reradiated field, i.e., the fields reradiated by the superradiant and subradiant mode. In this particular case, the interference of these fields is destructive, giving rise to an apparent *transparency* of the heptamer in scattering around the frequency where the subradiant mode is efficiently driven. As the phase of the response of the subradiant mode actually sweeps through 180^{o} as the frequency is swept through resonance, this interference reverses sign from constructive in the red part of the spectrum, to destructive in the blue part of the spectrum, as is evident when we compare the extinction in the presence and absence of the subradiant mode (dashed line in Fig. 3.13b). Due to the fact that interference between a broad and a narrow contribution is hidden in this scattering spectrum, the transparency window has been likened to 'electromagnetically induced transparency', as well as to the mathematics of Fano interference. Fano interference is the phenomenon that in any system of coupled oscillators with a broad and a narrow oscillator, the response to driving either one of the oscillators can show dispersive non-Lorentzian lineshapes as a consequence of a change from constructive to destructive interference in interaction with the second oscillator. The remarkably narrow plasmonic lineshapes of Fano interference due to plasmonic dark modes are attractive for sensing and spectroscopy applications, especially given that at transparency a substantial excitation energy is in the near-field, i.e. in the subradiant resonance.

3.5.4 Narrow Gaps Yield High Fields

For separations larger than a few nanometers, the dimer plasmons are well described by classical electromagnetic theory and field enhancements depend on the material, size and spacing of the particles. In the examples for single NPs and NP clusters that we have discussed so far, the field strength right at the interface of the metal is not exceedingly large. According to Eq. (3.13) the field strength right at the interface of a metal NP compared to the incident field strength $|E_{in}|$, is

approximately $3V\omega_0/\gamma r^3 \approx 4\pi\omega_0/\gamma$, which at optical frequencies amounts to about 10–50, depending on the choice of metal. Generally, improvements do occur with elongated NPs, giving rise to somewhat higher field enhancements at the sharpest ends. According to the simple plasmon hybridization theory outlined in Sect. 3.5.1, the field that is expected inside the gap of a plasmon dimer may exceed the single NP value by at most a factor 2 or so. If we examine a rigorous classical electrodynamic calculation of the electric field induced in a plasmon dimer when exciting it on resonance with the bonding mode, we indeed find a field enhancement in the gap that is larger than that for a single NP. Surprisingly, the enhancement significantly exceeds that predicted by the simple dipole model: the enhancement in fact reaches very high values that diverge to infinity for zero gap size in between the particles.

This observation points at the fact that a dipole approximation fails to describe the response of plasmon NPs when they are very close to each other. The approximately dipolar response of metal NPs in Sect. 3.3 was derived on the assumption that the driving fields are constant over the particle size. When the driving field has a strong gradient, multipoles are induced as well. For plasmon NPs such multipoles become increasingly important as the gap between NPs becomes less than their radius. In this regime, at very small separation, a large field enhancement occurs over a very small spatial range confined to the gap, corresponding to excitation of very high order multipoles. While the singular nature of touching geometries and sharp asperities make a general scaling argument to estimate field enhancements difficult, classical electrodynamic numerical simulations have shown that field enhancements $|E|/|E_0|$ of 100–1,000 times compared to the incident field strength can be reached in realistic scenarios, taking into account the radiative and Ohmic losses of metals. For gaps below 1 nm, quantum mechanical effects such as electron tunneling across the dimer junction and screening [37] significantly modify the optical response and drastically reduce the electromagnetic field enhancements relative to classical predictions, removing the divergence that occurs at zero separation. The high field-enhancements have been among the main drivers in the plasmon field, as they would allow spectroscopies such as Raman spectroscopy, which are characterized by weak signals that are very often masked by unwanted strong signals (e.g., fluorescence of the specimen), to be enhanced by many orders of magnitude. While the actual mechanisms that underlie so-called Surface Enhanced Raman Spectroscopy (SERS) on plasmon substrates are still under debate, there is consensus that high electric field enhancement in narrow gaps of up to $|E|^2/|E_0|^2 \sim 10^4$ or above can be routinely achieved.

By way of illustration, we discuss two examples of the use of plasmon oligomers, both shown in Fig. 3.14. The first concerns the well-known 'bowtie' antenna [38], that consists of two triangular metal particles in a bowtie arrangement, with a narrow gap in between them. Bowtie antennas combine the electromagnetic properties of sharp metal tips with those of coupled plasmon resonant NP pairs [30]. A closely related geometry is an antenna consisting of two metal nanorods placed tip-to-tip [39]. The coupling between the plasmon resonances in these geometries induces field enhancements in the gap region of up to 1,000. Such bowties can be

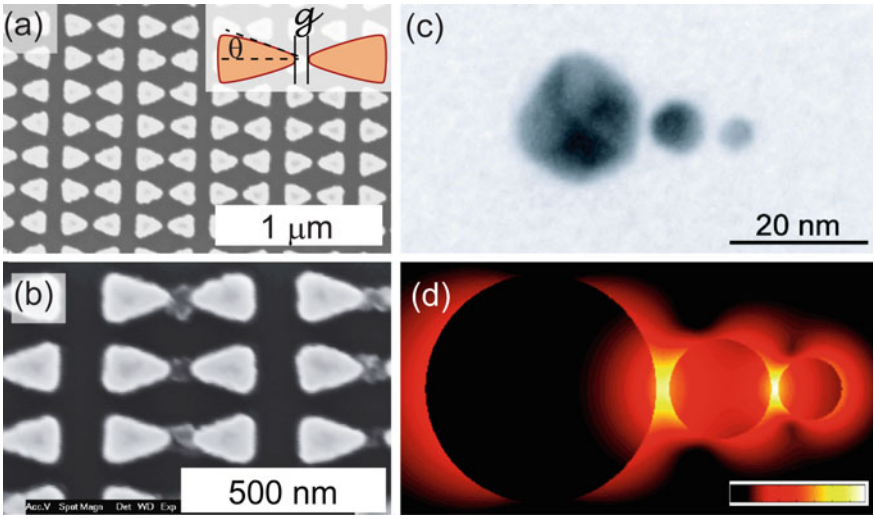

Fig. 3.14 Antenna geometries. *Left* SEM image of an array of bowtie antennas. In panel **b** we have visualized the field enhancement using a photopolymerizable resist (SU8 in this example). After exposure and development of the resist, polymer remains at the hot spots, i.e., in the antenna gaps. *Right panels* TEM image of a three-NP antenna created by functionalizing three Au NPs with complementary DNA strands. Hybridization of the strands allows selective formation of trimers with NPs of 20, 8 and 5 nm size, and 1–2 nm gaps. An electromagnetic simulation of the field intensity (|E|^2, on a logarithmic color scale covering 4 orders of magnitude) shows a tightly confined hotspot with 10^4 times enhancement of |E|^2. Note how inhomogeneous the field is inside the particles, evidencing that high order multipoles are at play. Panels (a, b) are modified with permission from [38], Copyright (2011) Optical Society of America. Panels (c, d) are reprinted with permission from [40], Copyright (2008) American Chemical Society

fabricated using state-of-the-art top-down lithography techniques with gaps that can reproducibly be smaller than 20 nm. Consistent with the ideas of plasmon hybridization, such antennas have a very strong response to incident light when excited with light polarized along the bowtie axis. The excitation drives the symmetric bright antenna mode, which is resonant typically at around 800 nm for gold bowties of $\sim$300 nm overall size. This resonance is red-shifted from that of the individual triangles, due to the elongated single particle shape and the longitudinal dipole moment alignment. The charge separation across the narrow gap implies that a very strong electric field is generated in the gap region. The high field enhancement of bowtie antennas has been evidenced in a set of experiments that include plasmon enhanced Raman scattering, fluorescence lifetime control, and the usage of bowtie antennas as near field scanning probes.

Instead of top-down lithographic fabrication of nano-antennas, an alternative approach uses self-assembly of colloidal NPs that have been synthesized in solution. A major advantage of using colloidal NPs for bottom-up fabrication of antennas is the crystalline nature of the NPs. The (near) absence of crystal defects reduces electron scattering and minimizes the additional damping of the plasmon oscillation. This can

result in higher field enhancements compared to lithographically fabricated structures, which are typically polycrystalline or amorphous. For example, experiments on an individual single-crystalline Au nanorod have shown fluorescence enhancements larger than 1,000-fold for single dye molecules (Sect. 3.4.5).

To achieve even higher enhancements, antennas consisting of multiple colloidal NPs can be assembled in solution and subsequently deposited on a substrate. Using thiol-linkers, Au NPs can be functionalized with single stranded DNA. By functionalizing NPs with complementary strands, oligomers of controlled composition can be formed, where the spacing between the NPs is set by the length of the DNA strand (on the order of 5 nm). For instance, this approach was used by Bidault et al. [40] to construct plasmon trimers consisting of Au NPs of diameter 20, 8 and 5 nm attached in a linear string with gaps of just 1–2 nm. The excitation of the large NP is converted into a strong hot spot in the gap with the next smaller NP. By virtue of the self-similarity, an even stronger hot spot is found in the opposing gap at the smallest NP. According to electrodynamic calculations, the field enhancement in the 1–2 nm gaps can be as high as 100, corresponding to a 10^4 times enhancement. Recent measurements of spontaneous emission of dye molecules localized in the gap [41] confirm the presence of very strongly enhanced fields. The compatibility of Au with DNA chemistry and the emergence of techniques like DNA origami means that arbitrary scaffolds for bottom-up fabrication of plasmon structures with ultrasmall gaps can be created.

3.5.5 Directional Scattering

As discussed above, plasmon oligomers are often called 'optical antennas' and likened to radio antennas. A large benefit of radio antennas is that they provide *directionality* to the process of sending and receiving radiowave signals. Plasmonic antennas can likewise impart directionality to emission and absorption of photons by single molecules, and other emitters such as semiconductor nanocrystals. To understand the physics, let us revisit the workings of the archetypical antenna for radio/TV waves that was designed by Yagi and Uda, which is treated in many antenna handbooks [42] and depicted in Fig. 3.15. The Yagi-Uda antenna consists of a set of dipolar scatterers that surround a single active element, i.e. a single current-carrying wire. The total size of a Yagi-Uda antenna is a few wavelengths, while the pitch between the elements is approximately λ/3. Scaled to optical frequencies, a Yagi-Uda antenna would hence be approximately 1 micron in size, and consist of plasmon NPs at pitches of 150 nm or so.

Let us try to assess how directionality comes about in such an array antenna. In the far zone, the field of N dipoles is the sum of far field dipole radiation of each scatterer. Let us consider a chain of N dipoles at equidistant separations d along the x axis, and with dipole moments of equal magnitudes $|\boldsymbol{p}|$ but different phases φ_m excited along the z-axis. In this case the far field factorizes as a spherical wave $\frac{e^{ikR}}{R}$,

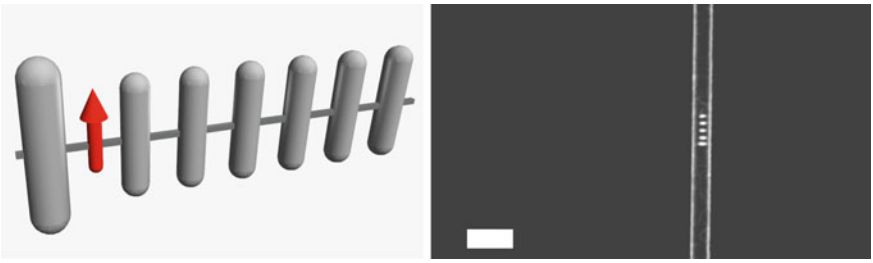

Fig. 3.15 *Left* cartoon of a Yagi-Uda antenna. For radio and TV waves such an antenna is meter sized, and consists of a single active element (*red arrow*, connected to current receiver/source) and a set of rods mounted on a linear mechanical support (thin rod). The vertical rods are cut to approximately λ/4 length, and the antenna pitch is at most λ/3. The longer rod is called 'reflector', while the set of smaller rods are called 'directors'. When driven (current through red element, which alone would be an isotropic radiator), the antenna radiates strongly along the axis of the antenna while no radiation emerges on the reflector side. *Right* scanning electron micrograph of a Yagi-Uda antenna with a response at optical wavelengths. The total length of the structure is just 1 micron. The five gold NPs (reflector on lower side of antenna) are fabricated using electron beam lithography on top of an optical waveguide, which is a 500 nm wide silicon nitride strip on a quartz surface. The antenna can interface nanoscale sources and detectors to guided modes that propagate in the dielectric strip

multiplied by the radiation pattern specific to z-oriented dipoles, multiplied by a *structure factor*

$$S = \sum_{m=1}^{N} e^{ik\hat{\boldsymbol{r}}\cdot\boldsymbol{r}_m} e^{i\varphi_m} \tag{3.27}$$

that accounts for the coherent addition of radiation of the N dipoles. The coherent addition contains both geometrical phase differences $e^{ik\hat{\boldsymbol{r}}\cdot\boldsymbol{r}_m}$ and the phase differences φ_m. Suppose for instance that one would be able to excite the N plasmon NPs with phase differences that increase linearly from element to element by an amount βd such that $\varphi_m = \beta m d$. At a viewing angle θ relative to the x-axis, the structure factor yields

$$|S|^2 = \left| \sum_{m=1}^{N} e^{imd[k\cos\theta+\beta]} \right|^2 = \left[\frac{\sin\frac{N}{2} d[k\cos\theta+\beta]}{\sin\frac{1}{2} d[k\cos\theta+\beta} \right]^2 . \tag{3.28}$$

This structure factor is very strongly peaked in a particular direction, namely the direction set by $k\cos\theta + \beta = 0$, especially when many elements are present. Figure 3.16 shows the structure factor for different array lengths. The sharpness of the structure factor around the peak emission angle increases with the number of dipoles N in the array, allowing for very narrow beams using long arrays. The reasoning outlined above for the radiation pattern of coherently radiating dipoles is commonly used as a design tool in radio antenna engineering. In radio antenna

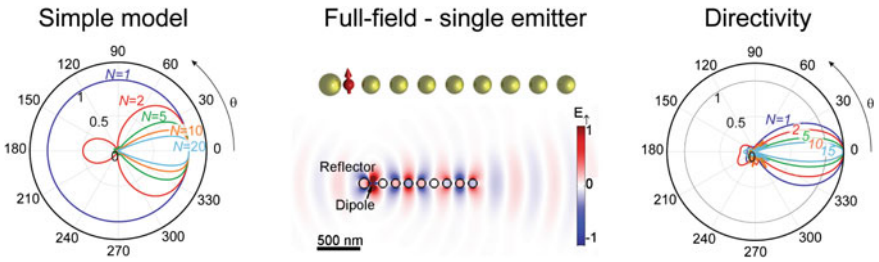

Fig. 3.16 (*Left panel*) Polar plot of the structure factor in Eq. (3.28) for a phased array in which the phase advance βd (with d the array pitch) from one dipole to the next is chosen exactly such that βd = kd = 2πd/λ. A single source is an isotropic emitter that radiates equally into all angles. A strong forward lobe develops for growing number of dipoles N. The angle θ is measured relative to the antenna axis. (*Center panel*) Electromagnetic field generated by a single emitter (radiating point dipole representing a single molecule) inside a plasmon antenna consisting of Au NPs embedded in a glass matrix, assuming a NP size of 100 nm and pitch of 150 nm. The field clearly shows that all NPs in the array are excited and carry large dipole moments, with a phase difference from NP to NP commensurate with the free space wavelength. The radiation of all these dipole moments plus that of the molecule itself add together in the far field to give a directional radiation pattern. (*Right panel*) Polar plot of the radiated intensity versus angle relative to the antenna axis for various numbers N of director NPs (note that there is always a reflector). Beyond N = 10 the radiation pattern does not improve further, as the number of NPs that the molecule can drive is limited. Figure adapted with permission from [46]

engineering, very often one can actually realize driving electronics that rigorously imposes a phase and amplitude on each of *N* dipoles in an array by controlling the magnitude and relative phase of currents driving each radiating wire in the radio antenna. No such luxury is available in plasmonics, as optics only allows a few distinct forms of driving, namely either by a local point source in the form of a fluorescent emitter, or in the form of an externally supplied incident beam. Controlling the phase of individual elements directly is hence impossible, since multiple fluorescent sources would not be coherent. However, the essence of plasmon antennas is that metal NPs that are near each other couple via dipole-dipole coupling. If we embed a single fluorophore in an array of NPs, it drives not only the metal NP that it is closest to, but the whole NP chain is excited. The field from the molecule, plus radiation from all the plasmon NPs finally need to be added together, and a directional radiation pattern ensues. In such a scenario the control parameters are firstly the choice of distances between NPs, and secondly a suitable choice of NP size and shape to engineer the magnitude and phase of the complex polarizability of each plasmon NP.

As discussed above, a particularly powerful example of the physics of such array antennas is the Yagi-Uda antenna [43–46]. Scaled to optical frequencies, it consists of a single emitter surrounded by a NP array. If the pitch of the array is chosen to be around a third of the operation wavelength, and the NPs are chosen to be just blue-shifted in resonance compared to the emitter, the molecule sets up a travelling wave in the NP array that has wave vector β almost equal to the free space wavelength. As a consequence, the antenna has a structure factor that is very highly peaked in

the forward direction, causing over 90 % of emission to be pointed in a forward lobe of small opening angle (around 20°). This type of optical antenna could be useful for creating single photon sources for secure quantum communication that are integrated in networks of dielectric waveguides. The benefit for microscopy on single molecules or single semiconductor nanocrystals, could be that fluorescence into a narrow radiation cone yields one to two orders of magnitude better collection efficiency, which would alleviate the need for expensive high NA microscope objectives. In principle, the antennas could be cheaply printed on a substrate using imprint nanolithography to replicate them from a lithographic master [47]. Thereby plasmon array antennas could potentially be useful to realize microscopy substrates that allow rapid fluorescence collection with cheap optics, and may improve the brightness of single photon sources that are based on single emitters. That the physics of Yagi-Uda plasmon antennas indeed works has been verified by Curto et al. [48]. In this experiment, Yagi-Uda antennas were fabricated on a glass slide, and one or a few quantum dots were lithographically grafted onto a single antenna element. The radiation pattern was found to be strongly peaked in a forward lobe. Due to the substrate, and contrary to the idealized calculation, this lobe is not, however, along the antenna axis, but points into the substrate under a 45° angle. While the structure factor for the Yagi-Uda antenna strongly peaks in the forward direction along the antenna axis, it is not sufficiently peaked to overcome the fact that on a substrate the single dipole radiation pattern is exceptionally strongly peaked into the direction of the critical angle (45° downwards into the glass).

The Yagi-Uda antenna is just one example of the usefulness of NP clusters to provide directivity to emission. Recently it has also been shown that 2D clusters of particles, as well as 2D clusters of holes in metal films, can similarly impart directionality on scattering and on emission by single fluorophores. The advantage of 2D systems is that directivity enhancement perpendicular to the substrate on which the cluster is deposited can be achieved, making such structures useful for fluorescence enhancement in microscopy applications. In general, current efforts in this direction use lithographically prepared structures because lithography allows to make structures with controlled dimensions (down to 5 nm error) at the required overall sizes that are approximately twice the wavelength (total size 1 or 2 μm). In principle, assembly of linear chains of metal NPs with a single emitter at a controlled location could also be possible using self-assembly techniques.

3.5.6 Lattices of Plasmonic Particles

Finally, we discuss infinite periodic lattices of plasmon scatterers. From our review of finite plasmon NP clusters, it is evident that arraying multiple objects together allows to sharpen resonances, shift resonances, and to obtain very high directionality. In particular, we mention the possibility to enhance sensing and spectroscopy through collective lattice resonances. The new physics in lattices compared to that of finite clusters is the appearance of very sharp optical features that are well known

in the physics of gratings as 'Wood's anomalies' and 'Rayleigh anomalies'. In the context of plasmonics these types of effects have been studied both in systems composed of metal particles in a transparent background, and in systems that possess the inverse geometry, i.e. holes perforated in thin metal films. This second case has opened the new field of 'Extraordinary Optical Transmission' spawned by the pioneering work of Ebbesen [49], but falls outside the scope of this book. We refer the reader to reviews on this subject [50, 51]. Here we discuss periodic arrays of plasmon NPs, a subject first studied in detail by the groups of Schatz and Van Duyne, and by Rivas et al. [52, 53].

The physics of two-dimensional periodic systems of NPs is best appreciated by turning once again to a point dipole model. Suppose that we have a lattice of identical NPs located on sites $\boldsymbol{r}_{pq} = p\boldsymbol{a}_1 + q\boldsymbol{a}_2$ where $\boldsymbol{a}_{1,2}$ are basis vector, and p, q are both integers. If the lattice is illuminated under normal incidence, this will cause all the polarizable particles to obtain the *same* dipole moment. This dipole moment is once again given by the incident field, plus the field of all dipoles in the lattice, such that (with θ_{pq} the angle between the induced moments $\boldsymbol{p}$ and the vectors $\boldsymbol{r}_p - \boldsymbol{r}_q$)

$$p = \alpha(\omega)\left[\boldsymbol{E}_{in} + \sum_{p\neq q} e^{ikr_{pq}}\left[\frac{3\cos^2\theta_{pq}-1}{4\pi\varepsilon_0 r_{pq}^3}\left(1-ikr_{pq}\right) + k^2\frac{\sin^2\theta_{pq}}{4\pi\varepsilon_0 r_{pq}}\right]p\right]. \quad (3.29)$$

This equation can be rewritten as

$$p = A(\omega)\boldsymbol{E}_{in},$$

with

$$A(\omega) = \frac{1}{1/\alpha(\omega) - S}, \quad (3.30)$$

i.e., as if we deal with a lattice of uncoupled particles, but with a renormalized polarizability $A(\omega)$that is determined by interactions in the lattice quantified by the lattice sum S

$$S = \sum_{p\neq q} e^{ikr_{pq}}\left[\frac{3\cos^2\theta_{pq}-1}{4\pi\varepsilon_0 r_{pq}^3}\left(1-ikr_{pq}\right) + k^2\frac{\sin^2\theta_{pq}}{4\pi\varepsilon_0 r_{pq}}\right]. \quad (3.31)$$

Note how the lattice sum S depends on the lattice geometry but *not* on any property of the single NPs. In case of oblique incidence with parallel wave vector $\boldsymbol{k}_{|,\mathrm{in}}$, i.e. under angle θ = asin ($|\boldsymbol{k}_{|,\mathrm{in}}|/k$), the phase factor $e^{ikr_{pq}}$ in the lattice summands is further modified to read $e^{ikr_{pq}+\boldsymbol{k}_{\|,\mathrm{in}}\boldsymbol{r}_{pq}}$. The lattice sum is not entirely trivial to calculate, as it requires a technique borrowed from solid state physics called 'Ewald lattice summation'. Indeed, readers may recognize the lattice summations from the well-

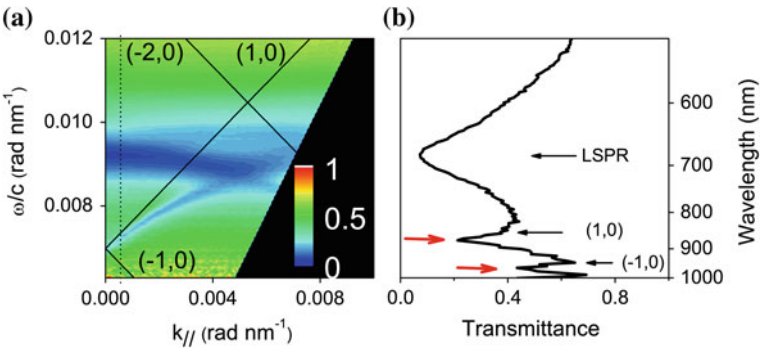

Fig. 3.17 Measured extinction for a lattice of plasmonic nanorods excited along their long axis as a function of incidence angle ($k_{//} = 2\pi/\lambda \sin\theta$) and incident wavelength. Panel B shows a cross cut at normal incidence. Figure reprinted with permission from [53], Copyright (2009) by The American Physical Society

known summation of electrostatic dipole interactions that occurs in evaluating Madelung constants.

An example of the measured extinction through a square grating of plasmon NPs on a substrate is shown in Fig. 3.17 as a function of wavelength ($2\pi/\lambda$ on the vertical axis) and incidence angle (actually $2\pi/\lambda\sin\theta$) on the horizontal axis. The measurement shows two distinct features. Firstly at around 680 nm wavelength (0.0092 rad/nm) a broad almost angle independent band appears in which transmission is suppressed. This band corresponds to the single NP resonance and is due to the resonance in $\alpha(\omega)$. Secondly, a narrow line crosses obliquely through the diagram. This narrow line is contributed by the lattice sum S, and occurs exactly when the lattice allows diffraction of the incident beam into a diffracted beam that lies in the lattice plane. Importantly, the lattice sum is strongly structured near each of these diffraction conditions, and furthermore is a *complex* quantity with both a real and an imaginary part. The real part causes the resonances of the array, i.e., the collective hybridized mode frequencies, to be shifted compared to the single NP plasmon resonance at each crossing between the angle-independent plasmon band and the angle-dependent resonances in S. The imaginary part of the lattice sum can cause a change in linewidth of the collective lattice plasmon resonance. For lattices with pitch *below* half the wavelength, i.e., lattices so dense that no grating diffraction can occur, the radiative damping is typically larger than that of single scatterers. This is caused by coherently oscillating dipoles that are in phase and are superradiantly damped, in analogy to the bright plasmon modes of a dimer (Sect. 3.5.2).

Remarkably, under certain conditions the lattice sum can completely cancel the radiative damping of the plasmon particle, giving rise to narrowing of resonance features. The physics is that just prior to the emergence of a diffraction order, the lattice supports a bound mode that is delocalized in 2D over the entire lattice, but bound in the third dimension. Since a significant proportion of the electromagnetic

field energy resides just *outside* the metal NPs, the loss rate is even lower than the Ohmic damping rate of the metal, giving rise to very sharp resonances.

Surface lattice resonances in 2D plasmonic arrays are pursued for a variety of applications. In optical sensing, the sensitivity is often expressed as a figure-of-merit (FOM) according to Eq. (3.21) that we defined for a single particle plasmon sensor. The FOM is greatly boosted for arrays by the fact that resonance lines can have a linewidth that is an order of magnitude below that of single NPs. Thereby 2D plasmonic arrays are very suited to measure surface covering layers of analytes that present a small index difference. In Sect. 3.4.4 we saw that single plasmon NP sensing can even register the binding and unbinding of single proteins through a resonance shift. In plasmon NP arrays this is fundamentally impossible, as one relies on probing an extended area. Nonetheless, fractions of a monolayer of deposited material can be in principle detected as a resonance shift.

Advantageously, large field enhancements outside the NP can be obtained due to the collective lattice resonance effect. Indeed, the first pursuits of plasmon lattices were focused on realizing substrates for reproducible SERS measurements. The groups of Schatz and Van Duyne were among the first to propose that so-called Fischer patterns, regularly used in the scanning probe microscopy community as topographical calibration samples, could be used for this purpose. Fischer patterns are obtained by first growing self-assembled hexagonally ordered close-packed monolayers of colloidal NPs on a glass substrate, and subsequently evaporating metal through the voids. Very reproducibly, a lattice of triangular particles with sharp tips and arranged in a pattern with hexagonal symmetry inherited from the colloidal lattice results. SERS signals from sub-monolayers of molecules (e.g. the DNA base adenine in [54]) can be obtained reproducibly in this manner.

Plasmonic lattices have also attracted interest as structures to improve the in- and outcoupling of light into high-index semiconductor structures. For instance, in the large emerging technology of solid state lighting, materials such as GaN and InGaN form the basis of powerful Light Emitting Diodes (LEDs). A significant problem in such LEDs is that the light is generated in a layer with very high refractive index (well above 2). Since the angle of incidence on the interface normal beyond which total internal reflection of light occurs is small for high refractive indices, most of the generated light is trapped, unless roughness or scattering layers are used to improve light outcoupling. Diffractive plasmonic lattices can be easily fabricated using for instance nano-imprint lithography on top of LED surfaces. The specific angle- and wavelength dependent resonances of such surface texturing can then be used to improve overall light extraction from LEDs for particular colors, as well as causing a redistribution of emitted light into particular emission angles. These strategies likewise extend to organic light emitting diode layers, where plasmon lattices help to enhance spontaneous emission decay rates.

Conversely to the case of improving light emitting devices, plasmon lattices have also been proposed for improving absorption of light by placing a lattice directly on top of, e.g., silicon photodiodes. Owing to their ability to redirect light via diffraction, plasmonic lattices increase the overall efficiency of thin photovoltaic cells [55]. Also, by suitable engineering of the shape resonances of the individual

particles narrowband color filter arrays have been fabricated directly onto the pixels of CMOS camera devices [56].

3.6 Exercises

1. Drude model for silver:
   (a) Calculate the plasma frequency from the electron density of silver.
   (b) What is the Drude damping rate, given the conductivity of silver at DC?
   (c) Prove that the polarizability of a silver sphere is a Lorentzian resonance.
   (d) Prove that inclusion of radiation damping (3.16) is formally equivalent to adding extra damping to the Ohmic damping. How large is the extra damping term? Plot the linewidth of the resonance as a function of particle diameter
   (e) Prove that the optical theorem holds if you use the polarizability of Eq. (3.16) in the limit of zero Ohmic damping: Scattering cross section = extinction cross section
   (f) Plot the "albedo", as a function of particle size, using the damping rate from (b), on resonance. The albedo (latin for "whiteness") denotes the ratio of scattering to extinction.
2. Silicon is a semiconductor that can be doped with both electrons and holes either by implanting donor/acceptor species, or by creating carriers thermally.
   (a) Suppose we consider n-type dopes silicon. What level of doping do we need to obtain a plasma frequency of 1 THz? Is this level of doping realistic?
   (b) For what size of particle is the dipole approximation still reasonable?
   (c) Plot the extinction cross section of an n-doped Si sphere with the doping from (a) and the size from exercise (b).
3. The optical properties of gold nanorods (which can be synthesized in large quantities in solution) are often approximated by assuming the shape to be prolate spheroidal (semi-major axis a, two equal semi-minor axes $b = c$).
   (a) Calculate the plasma frequency of gold. How does it compare to the plasma frequency for silver found in (1a)?
   (b) Plot the depolarization factors $L_{1,2,3}$ in the range of aspect ratios 1…5. What is the depolarization factor for an aspect ratio of 1, i.e. a sphere?
   (c) Calculate the scattering and extinction cross sections of a prolate spheroid with $a = 30$ nm and $b = c = 10$ nm, immersed in water (n = 1.33). Use the

Drude dielectric function for gold without radiation damping (see the caption of Fig. 3.1 for the relevant Drude parameters).

(d) How does the linewidth of this spheroid plasmon compare to the scattering linewidth of the 80 nm spherical particle plotted in Fig. 3.2b? What causes the broader linewidth for the sphere?

4. A single metal particle as a plasmonic biosensor.

(a) What determines the figure-of-merit (FOM) of a plasmon biosensor? Which shape gold particle would have a higher FOM, a sphere or a prolate spheroid with aspect ratio 4? Is the same true for silver?

(b) Assuming a Drude dielectric function, calculate the plasmon wavelength in the scattering spectrum for a gold prolate spheroid immersed in water (n = 1.33) with a semi-major axis of 20 nm and a semi-minor axis of 5 nm. Repeat the calculation for the same spheroid immersed in ethanol (n = 1.36).

(c) Calculate the FOM for this spheroid (Eq. 3.21).

5. Consider a dimer of two identically sized particles of volume V, at distance d. We use a Lorentzian expression for the polarizability and consider longitudinal coupling, as in Eq. 3.25

(a) Convince yourself that Eq. 3.25 is correct.

(b) In the text we set damping to zero to derive the resonances, and ignored radiation damping. The resonances are found by taking the determinant of the coupling matrix M (LHS of Eq. 3.25), and finding the roots. Here we consider a simple method to judge resonances in hybridization *including* damping. We use normalized units with $\omega_{SPR} = 1$, $\gamma_{Ohmic} = 0.01\ \omega_{SPR}$, V = 0.1 (meaning $V = 0.1(c/\omega_{SPR})^3$). Use a program such as Matlab, Octave or Mathematica to plot $1/|\det(M)|$ for various values of d between $\lambda/2\pi$ and $3\lambda/2\pi$ (i.e. d = 1 and 3 in normalized units) for frequencies from $0.5\ \omega_{SPR}$ to $1.5\ \omega_{SPR}$. Explain the resulting diagrams. What is the width of each peak?

(c) Now we introduce radiation damping through Eq. (3.16), which is equivalent to replacing the damping rate γ with

$$\gamma_{Ohmic} + 2/3\,\omega^2[V(\omega_{SPR})^2/c^3] = \omega_{SPR}[\gamma_{Ohmic} + 2/3\,(\omega/\omega_{SPR})^2[V(\omega_{SPR})^3/c^3]\,.$$

In our normalized units this means γ is replaced by $\gamma = 0.01 + 0.0667\,(\omega/\omega_{SPR})^2$. Again plot the absolute value of the inverse determinant. What happens to the peak height and width compared to c?

(d) In Fig. 3.12, which plots the response of a dimer upon plane wave excitation, the blueshifted mode is hardly visible. However, in (d), the blueshifted mode appears as a very narrow strong peak. Why does the blue-shifted

mode not appear in plane wave driving? Would it appear under other forms of driving?

References

1. Mie, G.: Beiträge zur Optik trüber Medien, speziell kolloidaler Metallösungen. Ann. Phys. **330**, 377–445 (1908)
2. Kreibig, U., Vollmer, M.: Optical Properties of Metal Clusters. Springer-Verlag, Berlin (1995)
3. Ashcroft, N.W., Mermin, N.D.: Solid State Physics. Brooks Cole (1976)
4. Johnson, P.B., Christy, R.W.: Optical constants of the noble metals. Phys. Rev. B. **6**, 4370–7379 (1972)
5. Palik, E.D.: Handbook of Optical Constants of Solids. Academic Press, Boston (1998)
6. Bohren, C.F., Huffman, D.R.: Absorption and Scattering of Light by Small Particles. Wiley-VCH, Weinheim (1998)
7. Kelly, K.L., Coronado, E., Zhao, L.L., Schatz, G.C.: The optical properties of metal nanoparticles: the influence of size, shape, and dielectric environment. J. Phys. Chem. B. **107**, 668–677 (2003)
8. Osborn, J.A.: Demagnetizing factors of the general ellipsoid. Phys. Rev. **67**, 351–357 (1945)
9. Sönnichsen, C., Franzl, T., Wilk, T., Von Plessen, G., Feldmann, J., Wilson, O., Mulvaney, P.: Drastic reduction of plasmon damping in gold nanorods. Phys. Rev. Lett. **88**, 77402 (2002)
10. Zijlstra, P., Orrit, M.: Single metal nanoparticles: optical detection, spectroscopy and applications. Rep. Progr. Phys. **74**, 106401 (2011)
11. Yguerabide, J., Yguerabide, E.E.: Light-scattering submicroscopic particles as highly fluorescent analogs and their use as tracer labels in clinical and biological applications—I. Theory. Anal. Biochem. **262**, 137–156 (1998)
12. Klar, T., Perner, M., Grosse, S., Von Plessen, G., Spirkl, W., Feldmann, J.: Surface-plasmon resonances in single metallic nanoparticles. Phys. Rev. Lett. **80**, 4249–4252 (1998)
13. McMahon, J.A., Wang, Y.M., Sherry, L.J., Van Duyne, R.P., Marks, L.D., Gray, S.K., Schatz, G.C.: Correlating the structure, optical spectra, and electrodynamics of single silver nanocubes. J. Phys. Chem. C **113**, 2731–2735 (2009)
14. Lindfors, K., Kalkbrenner, T., Stoller, P., Sandoghdar, V.: Detection and spectroscopy of gold nanoparticles using supercontinuum white light confocal microscopy. Phys. Rev. Lett. **93**, 37401 (2004)
15. Boyer, D., Tamarat, P., Maali, A., Lounis, B., Orrit, M.: Photothermal imaging of nanometer-sized metal particles among scatterers. Science **297**, 1160–1163 (2002)
16. Mooradian, A.: Photoluminescence of metals. Phys. Rev. Lett. **22**, 185–187 (1969)
17. Fujiwara, T., Ritchie, K., Murakoshi, H., Jacobson, K., Kusumi, A.: Phospholipids undergo hop diffusion in compartmentalized cell membrane. J. Cell Biol. **157**, 1071–1081 (2002)
18. Lasne, D., Blab, G.A., Berciaud, S., Heine, M., Groc, L., Choquet, D., Cognet, L., Lounis, B.: Single nanoparticle photothermal tracking (SNaPT) of 5-nm gold beads in live cells. Biophys. J. **91**, 4598–4604 (2006)
19. Ruijgrok, P.V., Verhart, N., Zijlstra, P., Tchebotareva, A.L., Orrit, M.: Brownian fluctuations and heating of an optically aligned gold nanorod. Phys. Rev. Lett. **107**, 37401 (2011)
20. Kyrsting, A., Bendix, P.M., Stamou, D.G., Oddershede, L.B.: Heat profiling of three-dimensionally optically trapped gold nanoparticles using vesicle cargo release. Nano Lett. **11**, 888–892 (2011)
21. Seol, Y., Carpenter, A.E., Perkins, T.T.: Gold nanoparticles: enhanced optical trapping and sensitivity coupled with significant heating. Opt. Lett. **31**, 2429–2431 (2006)

22. Zijlstra, P., Paulo, P.M.R., Orrit, M.: Optical detection of single non-absorbing molecules using the surface plasmon resonance of a gold nanorod. Nature Nanotechnol. **7**, 379–382 (2012)
23. Ament, I., Prasad, J., Henkel, A., Schmachtel, S., Sönnichsen, C.: Single unlabeled protein detection on individual plasmonic nanoparticles. Nano Lett. **12**, 1092–1095 (2012)
24. Sannomiya, T., Hafner, C., Voros, J.: In situ sensing of single binding events by localized surface plasmon resonance. Nano Lett. **8**, 3450–3455 (2008)
25. Zijlstra, P., Paulo, P.M.R., Yu, K., Xu, Q.-H., Orrit, M.: Chemical interface damping in single gold nanorods and its near elimination by tip-specific functionalization. Angew. Chem. Int. Ed. **51**, 8352–8355 (2012)
26. Beeram, S.R., Zamborini, F.P.: Selective attachment of antibodies to the edges of gold nanostructures for enhanced localized surface plasmon resonance biosensing. J. Amer. Chem. Soc. **131**, 11689–11691 (2009)
27. Anger, P., Bharadwaj, P., Novotny, L.: Enhancement and quenching of single-molecule fluorescence. Phys. Rev. Lett. **96**, 113002 (2006)
28. Mertens, H., Koenderink, A.F., Polman, A.: Plasmon-enhanced luminescence near noble-metal nanospheres: comparison of exact theory and an improved Gersten and Nitzan model. Phys. Rev. B. **76**, 1–12 (2007)
29. Liu, M.Z., Guyot-Sionnest, P., Lee, T.W., Gray, S.K.: Optical properties of rodlike and bipyramidal gold nanoparticles from three-dimensional computations. Phys. Rev. B. **76**, 235428 (2007)
30. Kinkhabwala, A., Yu, Z.F., Fan, S.H., Avlasevich, Y., Mullen, K., Moerner, W.E.: Large single-molecule fluorescence enhancements produced by a bowtie nanoantenna. Nature Photon. **3**, 654–657 (2009)
31. Novotny, L., Stranick, S.J.: Near-field optical microscopy and spectroscopy with pointed probes. Ann. Rev. Phys. Chem. **57**, 303–331 (2006)
32. Prodan, E., Radloff, C., Halas, N.J., Nordlander, P.: A hybridization model for the plasmon response of complex nanostructures. Science **302**, 419–422 (2003)
33. García De Abajo, F.J.: Multiple scattering of radiation in clusters of dielectrics. Phys. Rev. B. **60**, 6086–6102 (1999)
34. Fan, J.A., Wu, C., Bao, K., Bao, J., Bardhan, R., Halas, N.J., Manoharan, V.N., Nordlander, P., Shvets, G., Capasso, F.: Self-assembled plasmonic nanoparticle clusters. Science **328**, 1135–1138 (2010)
35. Hentschel, M., Saliba, M., Vogelgesang, R., Giessen, H., Alivisatos, A.P., Liu, N.: Transition from isolated to collective modes in plasmonic oligomers. Nano Lett. **10**, 2721–2726 (2010)
36. Frimmer, M., Coenen, T., Koenderink, A.F.: Signature of a fano resonance in a plasmonic metamolecule's local density of optical states. Phys. Rev. Lett. **108**, 077404 (2012)
37. Zuloaga, J., Prodan, E., Nordlander, P.: Quantum description of the plasmon resonances of a nanoparticle dimer. Nano Lett. **9**, 887–891 (2009)
38. De Hoogh, A., Hommersom, B., Koenderink, A.F.: Wavelength-selective addressing of visible and near-infrared plasmon resonances for SU8 nanolithography. Opt. Express **19**, 11405–11414 (2011)
39. Muskens, O.L., Giannini, V., Sánchez-Gil, J.A., Gómez Rivas, J.: Strong enhancement of the radiative decay rate of emitters by single plasmonic nanoantennas. Nano Lett. **7**, 2871–2875 (2007)
40. Bidault, S., García De Abajo, F.J., Polman, A.: Plasmon-based nanolenses assembled on a well-defined DNA template. J. Amer. Chem. Soc. **130**, 2750–2751 (2008)
41. Busson, M.P., Rolly, B., Stout, B., Bonod, N., Bidault, S.: Accelerated single photon emission from dye molecule-driven nanoantennas assembled on DNA. Nature Commun. **3**, 962 (2012)
42. Balanis, C.A.: Antenna theory: Analysis and design. Wiley Asia (2005)

43. Hofmann, H.F., Kosako, T., Kadoya, Y.: Design parameters for a nano-optical Yagi-Uda antenna. New J. Phys. **9**, 217 (2007)
44. Li, J., Salandrino, A., Engheta, N.: Optical spectrometer at the nanoscale using optical Yagi-Uda nanoantennas. Phys. Rev. B. **79**, 195104 (2009)
45. Taminiau, T.H., Stefani, F.D., Van Hulst, N.F.: Enhanced directional excitation and emission of single emitters by a nano-optical Yagi-Uda antenna. Opt. Express **16**, 10858–10866 (2008)
46. Koenderink, A.F.: Plasmon nanoparticle array waveguides for single photon and single plasmon sources. Nano Lett. **9**, 4228–4233 (2009)
47. Ji, R., Hornung, M., Verschuuren, M.A., Van de Laar, R., Van Eekelen, J., Plachetka, U., Moeller, M., Moormann, C.: UV enhanced substrate conformal imprint lithography (UV-SCIL) technique for photonic crystals patterning in LED manufacturing. Microelectron. Eng. **87**, 963–967 (2010)
48. Curto, A.G., Volpe, G., Taminiau, T.H., Kreuzer, M.P., Quidant, R., Van Hulst, N.F.: Unidirectional Emission of a quantum dot coupled to a nanoantenna. Science **329**, 930–933 (2010)
49. Ebbesen, T.W., Lezec, H.J., Ghaemi, H.F., Thio, T., Wolff, P.A.: Theory of extraordinary optical transmission through subwavelength hole arrays. Nature **391**, 667–669 (1998)
50. García De Abajo, F.J.: Colloquium: light scattering by particle and hole arrays. Rev. Mod. Phys. **79**, 1267–1290 (2007)
51. Garcia-Vidal, F.J., Ebbesen, T.W., Kuipers, L.: Light passing through subwavelength apertures. Rev. Mod. Phys. **82**, 729–787 (2010)
52. Zou, S., Janel, N., Schatz, G.C.: Silver nanoparticle array structures that produce remarkably narrow plasmon lineshapes. J. Chem. Phys. **120**, 10871–10875 (2004)
53. Vecchi, G., Giannini, V., Gómez Rivas, J.: Shaping the Fluorescent emission by Lattice resonances in plasmonic crystals of nanoantennas. Phys. Rev. Lett. **102**, 146807 (2009)
54. Hennemann, L.E., Kolloch, A., Kern, A., Mihaljevic, J., Boneberg, J., Leiderer, P., Meixner, A.J., Zhang, D.: Assessing the plasmonics of gold nano-triangles with higher order laser modes. Beilstein J. Nanotechnol. **3**, 674–683 (2012)
55. Atwater, H.A., Polman, A.: Plasmonics for improved photovoltaic devices. Nature Mater. **9**, 205–213 (2010)
56. Yokogawa, S., Burgos, S.P., Atwater, H.A.: Plasmonic color filters for CMOS image sensor applications. Nano Lett. **12**, 4349–4354 (2012)